Supporting Information for "A metamorphic origin for Europa's ocean"

Mohit Melwani Daswani[1], Steven D. Vance[1], Matthew J. Mayne[2], Christopher R. Glein[3]

[1]Jet Propulsion Laboratory, California Institute of Technology, Pasadena, CA, USA
[2]Department of Earth Sciences, Stellenbosch University, RSA
[3]Space Science and Engineering Division, Southwest Research Institute, San Antonio, TX, USA

Contents

Corresponding author: M. Melwani Daswani, `mohit.melwani.daswani@jpl.caltech.edu`

Table S1: Review of reported post-*Galileo* nested spherical shell models for Europa

Analysis of gravitational coefficients inferred from *Galileo* radio science data permit only radial models of composition (Anderson et al., 1998; Zhang, 2003; Sotin & Tobie, 2004; Kuskov & Kronrod, 2005; Schubert et al., 2009; Vance et al., 2018). Such models are non-unique and subject to uncertainty about the bulk composition and mineralogy of the deep interior of Europa (e.g., Zolotov & Kargel, 2009), for which mantle and core densities must be assumed (e.g., Schubert et al., 2009). The following table summarizes plausible spherical shell models from the literature consistent with *Galileo* data.

Table 1. Review of reported post-*Galileo* nested spherical shell models for Europa.

Source	Core ρ kg/m^3	Core radius km	Mantle ρ kg/m^3	Mantle radius km	Ocean ρ kg/m^3	Ocean depth km	Ice ρ kg/m^3	Ice thickness km
A1998[a]	5150	0–827	3080–3800	660–1400	900–1300[b]	80–200[b]	[b]	[b]
A1998	8000	0–593	3000–3800	860–1400	900–1270[b]	80–200[b]	[b]	[b]
T2003[c]	5500	650	3500	1415	1000	120–130	920	20–30
H2004[d]	5150	599	3542	1421	1000	40–120	1000	20–100
K2005[e]	5700	555–660	3320–3400	1435–1450	$f(P,T)$ EOS	115–130[b]	$f(P,T)$ EOS	[b]
K2005	5700	505–630	3400–3480	1425–1440[f]	$f(P,T)$ EOS	125–140[b]	$f(P,T)$ EOS	[b]
K2005	5700	470–610	3450–3520	1425–1435	$f(P,T)$ EOS	130–140[b]	$f(P,T)$ EOS	[b]
K2005	4700	455–670	3600–3670	1405–1420[f]	$f(P,T)$ EOS	145–160[b]	$f(P,T)$ EOS	[b]
K2005	5700	560–670	3320–3400	1450–1465	$f(P,T)$ EOS	100–115[b]	$f(P,T)$ EOS	[b]
K2005	5700	510–640	3400–3480	1440–1460[f]	$f(P,T)$ EOS	105–125[b]	$f(P,T)$ EOS	[b]
K2005	5700	490–620	3450–3520	1440–1455	$f(P,T)$ EOS	110–125[b]	$f(P,T)$ EOS	[b]
K2005	4700	470–670	3600–3670	1425–1440[f]	$f(P,T)$ EOS	125–140[b]	$f(P,T)$ EOS	[b]
T2005[g]	5150		3300		1000		1000	
T2005	5150		3300		1000		1000	
T2005	8000		3300		1000		1000	
T2005	8000		3300		1000		1000	
S2009[h]	8000	706	2500	1561	1000[b]	0.7[b]		
S2009	4700	1012	2500	1529	1000[b]	33[b]		
S2009	8000	437	3500	1427	1000[b]	135[b]		
S2009	4700	702	3500	1425	1000[b]	137[b]		
S2009	8000	245	3760	1401	1000[b]	161[b]		
S2009	4700	409	3760	1401	1000[b]	162[b]		
V2018[i]	8000	479	3426	1428	1130	103		30
V2018	8000	478	3426	1426	1130[h]	131		5
V2018	8000	475	3427	1434	1020[h]	97		30
V2018	8000	476	3426	1433	1020[h]	124		5
V2018	8000	478	3427	1432	1060[h]	99		30
V2018	8000	478	3426	1431	1060[h]	126		5

[a]Anderson et al. (1998).

[b]Includes both liquid ocean and ice.

[c]Tobie, Choblet, and Sotin (2003).

[d]Hussmann and Spohn (2004).

[e]Kuskov and Kronrod (2005).

[f]Includes differentiated crust.

[g]Tobie, Mocquet, and Sotin (2005), for a generic Europa with mantle + core radius = 1600 km and average density = 3000 kg/m^3.

[h]Schubert et al. (2009). Silicate density and core density are independent variables.

[i]Vance et al. (2018). Ice thickness and core density are independent variables. Ocean density is a function of depth and composition of the ocean; mean values reported here are taken from Figure 7 in V2018.

Figure S1: Method flowchart

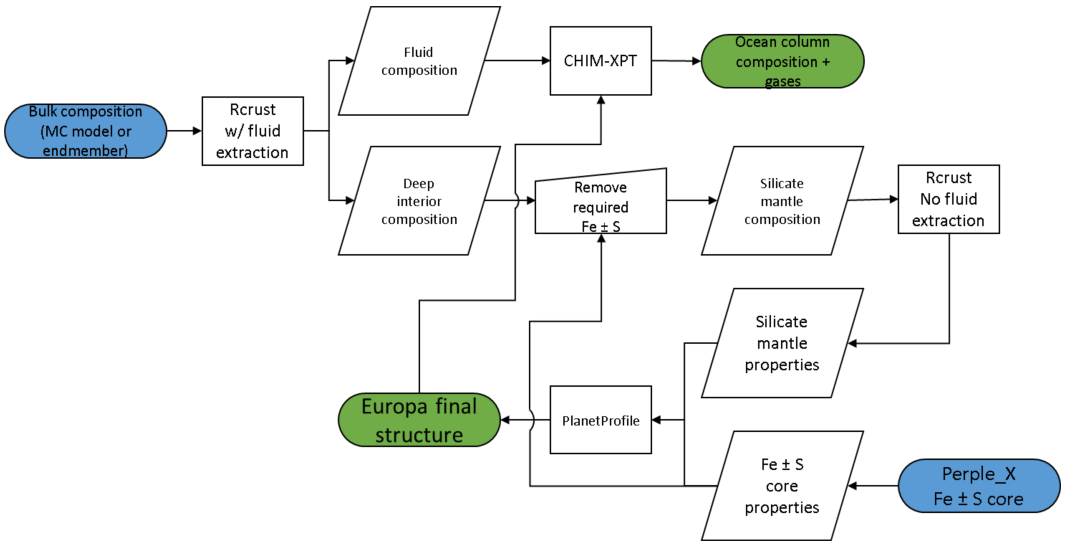

Figure 1. Method flowchart. Blue = start. Green = end results.

Table S2: Compositions of the satellitesimals used in the accretion model

Table 2. Adopted compositions of the satellitesimals used in the accreted composition model (*MC-Scale*), based on the compositions of carbonaceous chondrites and comet 67/Churyumov-Gerasimenko. Element concentrations in wt. %, total normalized to 100 wt. %. Compositions for chondrites are from Lodders and Fegley (1998), except for CI chondrites, which are from Palme et al. (2014). Chlorine concentrations for chondrites are from Clay et al. (2017). Comet 67P/Churyumov-Gerasimenko's composition and density is a synthesis from Pätzold et al. (2016); Dhooghe et al. (2017); Le Roy et al. (2015); Bardyn et al. (2017), using a dust-to-ice mass ratio of 4 from Pätzold et al. (2016). Densities of chondrites are from Flynn et al. (2018). Nitrogen in the resulting composition from the accretion model was not included in the input for the geochemical evolution model. Sulfate salts found in CI chondrites have been attributed to terrestrial alteration of native sulfides (Fredriksson & Kerridge, 1988; Airieau et al., 2005; Zolensky et al., 1993; Gounelle & Zolensky, 2001; Brearley, 2006), but note that: 1) the thermodynamic models are insensitive to initial mineralogy, and in fact predicts sulfides and not sulfates at initial equilibration (§, and Fig. S12–S13), and 2) the CI chondrite composition from Palme et al. (2014) represents a careful compilation of best values from multiple studies, compares excellently to solar photosphere abundances, and is a standard for CI chondrite compositions. Note that there is more uncertainty in the oxygen abundance of the solar photosphere than the CI chondrites (Palme et al., 2014).

Element (wt. %)	CI	CV	CM	CK	CR	CO	67P/C-G
H	2.006	0.287	1.428	0.285	0.319	0.071	11.283
C	3.543	0.544	2.244	0.224	2.038	0.447	27.814
N	0.300	0.008	0.155	0.008	0.063	0.009	1.021
O	46.737	37.980	44.073	39.802	39.280	37.578	41.652
Na	0.505	0.349	0.398	0.315	0.336	0.427	0.696
Mg	9.714	14.679	11.733	14.942	13.961	14.727	0.985
Al	0.855	1.725	1.153	1.494	1.172	1.422	0.178
Si	10.895	16.116	12.957	16.060	15.286	16.047	10.434
S	5.448	2.258	2.755	1.728	1.937	2.234	1.789
Cl	0.012	0.005	0.019	0.005	0.007	0.005	0.031
K	0.057	0.037	0.038	0.029	0.032	0.037	0.031
Ca	0.928	1.889	1.316	1.728	1.315	1.605	0.082
Fe	19.000	24.123	21.731	23.379	24.254	25.391	6.035
Density (kg/m^3)	1570	2970	2270	2900	3110	3100	533
Distance from Jupiter (AU)	12	0.6	0.76	0.6	0.84	0.72	12–27

Text S1: Additional details about the initial bulk composition models.

To establish what the composition (including water mass fraction) of the building blocks might have been, we use the hydrodynamic–geochemical sorting model of Desch, Kalyaan, and Alexander (2018), which provides an independent constraint on the distribution of materials in the early solar system, and specifically, the location of the formation of carbonaceous chondrites beyond the pressure bump created by Jupiter's formation. This pressure bump would have impeded the transport of non-carbonaceous material from the inner solar system to Jupiter's circumplanetary disk ($\sim$ 3 AU Desch et al., 2018). We assume that Europa's formation entailed preferential gravitational attraction of materials closest to its location, so we apply a Monte Carlo accretion model (*MC-Scale*) in which the prior probability of different accreting chondritic particle compositions is scaled by the reciprocal of their squared distance from Jupiter, according to the model by (Desch et al., 2018). We also include cometary satellitesimals. Compositions and formation distances for each of the compositional endmembers are given in Table S2.

We assume that Europa's mass and radius have not changed significantly since accretion. Here, the radius of the growing embryo of Europa scales with mass, modifying the power law from Sotin, Grasset, and Mocquet (2007) to fit Europa's current mass and radius[1]:

$$r_e = r_\oplus (1.072 (M_e/M_\oplus)^{0.306}) \tag{1}$$

where r_e and M_e are the radius and mass of Europa's embryo at any one time during accretion, and $r_\oplus$ and $M_\oplus$ are the radius and mass of Earth.

1. *MC-Scale*, where we assume that Europa's formation entailed preferential gravitational attraction of materials closest to its location (see Canup & Ward, 2009; Estrada et al., 2009; McKinnon & Zolensky, 2003). We carry out 10^4 iterations, where the probability of different chondritic satellitesimal compositions is scaled by their distance of formation beyond the pressure bump created by Jupiter's formation, according to the hydrodynamic/geochemical sorting model of Desch et al. (2018). We also consider cometary satellitesimals, which we assume form initially at 15–30 AU. The prior probability for accreting particle compositions is scaled by the reciprocal of their squared distance from Jupiter. Compositions and formation distances for each of the compositional endmembers are given in Table S2.
2. *EM-CI*, where the only satellitesimals are CI carbonaceous chondrites, which are the most water-rich chondrites. To explore the volatile evolution of a geochemically reduced but volatile-rich Europa, we additionally explored a hypothetical reduced CI chondrite at 2 log units below the Fayalite-Magnetite-Quartz redox buffer (FMQ$-$2).
3. *EM-CM*, where the only satellitesimals are CM carbonaceous chondrites.

The accretion model assumes a spherical Europa constructed with satellitesimals formed from uniform pebbles 0.005–0.5 m in radius, consistent with accretion from mostly dehydrated material (0–50 % water) of otherwise solar composition (i.e., approximately chondritic) inside of the circumjovian snowline (Ronnet et al., 2017). The small size of the pebbles matters because: 1) the impact energy of single particles will not raise the growing body's temperature to the extent that volatile loss during accretion is substantial, 2) small particles are less likely to have been thermally processed

[1] 4.80×10^{22} kg $\pm 1.26 \times 10^{20}$, and 1560.8 $\pm$ 0.5 km, respectively. Radius retrieved from NASA/JPL SSD (`https://ssd.jpl.nasa.gov/?sat_phys_par`). Mass calculated from GM (3202.739 $\pm$ 0.009 km^3/s^2) reported in the same source.

prior to accretion by the decay of short-lived radionuclides if accretion was protracted, and 3) the large number of pebbles required to form Europa's mass decreases the likelihood of statistical outliers dominating Europa's bulk composition. We use these simple models only to resolve the plausible range of initial bulk compositions—not the accretion process itself, nor the timing of Europa's formation beyond that implied by using known carbonaceous chondrite and comet compositions as building blocks. This assumption is reasonable because either the accretion of the jovian satellites (Canup & Ward, 2009) or the delivery of solids to the circumjovian disk (Estrada et al., 2009) were protracted. If the Galilean satellites formed earlier than the carbonaceous chondrites, the non-carbonaceous parent bodies of primitive achondrites that predated the formation of carbonaceous chondrites probably had a similar volatile content to carbonaceous chondrites (e.g., Day et al., 2019). The resulting initial bulk compositions are summarized in Table S3.

Table S3: Initial bulk compositions for *EM-CI*, *EM-CM* and *MC-Scale*

Table 3. Bulk initial compositions of Europa, post-accretion, used as inputs in the geochemical evolution models. Compositions based on CI and CM carbonaceous chondrites, and a Monte Carlo accretion model. The composition of the FMQ−2 CI chondrite (*EM-CI, FMQ−2*) is pressure dependent, calculated at 273 K, from 1 bar to 86700 bar, adjusting the oxygen concentration of *EM-CI* with the equilibrium expression $\log_{10} fO_2 = -26455.3/T + 8.344 + 0.092 \times ((P-1)/T)$), from Frost (1991), where T is temperature in K and P is pressure in bar. The composition for *EM-CI, FMQ−2* shows the minimum and maximum throughout the pressure range.

Element (wt. %)	*EM-CI*	*EM-CM*	*MC-Scale*	*EM-CI, FMQ−2*
H	2.01	1.43	0.391	2.421–2.562
C	3.56	2.25	0.874	4.288–4.537
O	46.92	44.14	39.360	32.365–36.071
Na	0.51	0.40	0.360	0.614–0.650
Mg	9.79	11.75	14.297	11.793–12.477
Al	0.87	1.15	1.452	1.048–1.109
Si	10.94	12.98	15.586	13.179–13.943
S	5.47	2.76	2.133	6.589–6.971
Cl	0.01	0.02	0.007	0.012–0.013
K	0.06	0.04	0.001	0.072–0.076
Ca	0.94	1.32	1.636	1.132–1.198
Fe	18.91	21.76	23.903	22.779–24.100

Text S2: Isobaric heating/prograde metamorphism fluid extraction model parameters

Buoyancy drives fluids away from Europa's center, with transport being particularly rapid in permeable materials in the direction of maximum compressive stress (e.g. Richard et al., 2007). Fluids resulting from mineral devolatilization increase pore fluid pressures (e.g. Leclère et al., 2018) which can propagate porosity waves under compaction (Connolly & Podladchikov, 1998), and also hydrofractures (e.g. Miller et al., 2003) and stresses that embrittle the overburden (Ferrand et al., 2017) and facilitate fluid migration. Gravitational settling of solids in Europa's interior creates resistance to deformation caused by increased pore fluid pressure, and this produces compaction pressure gradients that force fluids up through the most permeable paths. Focused channelization of fluids connecting disparate fluid production depths may also occur under compaction (Wilson et al., 2014; Miller et al., 2003), especially if the devolatilized fluid is less viscous than the medium. Retention of fluids at high pressure would lead to an unstable solution that is out of hydrostatic equilibrium. Thus, the only path for free low density fluids is up.

`Perple_X`

The composition and abundance of volatile elements released and extracted from the silicate interior during the thermal evolution of Europa were calculated using version 6.8.7 of the `Perple_X` Gibbs free energy minimization code (Connolly, 2009) together with a lagged speciation algorithm (Connolly & Galvez, 2018) and the Deep Earth Water model (DEW; Pan et al., 2013; Sverjensky et al., 2014) to quantify electrolytic fluids produced. We also use a generic hybrid molecular fluid equation of state model including CO_2-CH_4-H_2-CO-H_2O-H_2S-SO_2 fluid with non-linear subdivisions (COH-Fluid+). Activity-composition models, and solution model thermodynamic data for mineral phases and silicate melt phases were mainly selected from the "igneous set" implemented in `Perple_X`, adapted mainly from Holland, Green, and Powell (2018), shown in Table 4, and which is also used in the phase equilibrium software THERMOCALC. The "igneous set" of equations of state (the other two families are the "metapelite set" and the "metabasite set") is calibrated up to 6 GPa, and is the most appropriate for the pressure and temperature range, and the wide compositional space, explored here (García-Arias, 2020). For carbonates, we use the solution models Do(HP) and M(HP) derived from Holland, Baker, and Powell (1998), including the calcite ($CaCO_3$), aragonite ($CaCO_3$), magnesite ($MgCO_3$), dolomite ($CaMg(CO_3)_2$), ankerite ($CaFe(CO_3)_2$) and siderite ($FeCO_3$) endmembers. Some mineral, organic and melt end-members (e.g., fo8L, qjL) were excluded because of their incompatibility with the solution models used, or suspect stability. The h2oL melt end-member was also excluded because of overstabilizing melt at low temperature.

`Perple_X` has been used extensively to constrain the decarbonation and dehydration of mantle rocks and subducting crust on Earth, and validation of thermodynamic models and code are available in the literature. The most relevant calibration and validation of the dehydration and decarbonation reactions are found in Connolly (2005); Bjerga (2014); Bjerga, Konopásek, and Pedersen (2015); Bretscher, Hermann, and Pettke (2018). Gorce, Caddick, and Bodnar (2019) verified that thermodynamic models of decarbonation and dehydration with `Perple_X` approximate field volatile flux measurements closely: like in the models presented in this work, carbon release is facilitated by low to moderate temperature deserpentinization, or high temperature destabilization of carbonates. Recent tests with `Perple_X` for serpentine stability and the devolatilization of talc-carbonate rocks relevant to those presented in this work can be found in Nozaka, Wintsch, and Meyer (2017) and Menzel, Garrido, and López Sánchez-Vizcaíno (2020). `Perple_X` may underestimate the stability of hydrated phases at high pressure (6–8 GPa) and moderately high temperature (873–1073 K) (Cerpa et al., 2020),

but our differentiation thermodynamic models proceed to temperatures high enough ($\sim$ 1250 K) to offset dehydration overestimations at moderate temperatures.

`Rcrust`

The `Rcrust` program (version 2019-12-04) (Mayne et al., 2016) was used to calculate the isobaric prograde heating paths from 273.15 K up to 1473.15 K in 20 K increments (ΔT). No fluids were extracted at the 273.15 K isotherm to equilibrate the composition at all pressures initially; fluid extraction is first allowed to occur at the first temperature increment (293.15 K). At each depth (93 MPa increments from the surface to the core-silicate boundary) in the silicate interior, where pressure is assumed to remain constant, prograde reactions with increasing temperature are net fluid-producing, therefore fluids permeating from underlying layers are assumed to not have significant interactions with overlying layers, as fluids are already in excess. The spacing of the temperature and pressure increments was chosen to obtain accurate results while keeping model run times and output file sizes reasonable ($\lesssim$ 30 h and $\lesssim$ 1 GB respectively). Given the wide PT space explored here, the model PT spacing is reasonable in order to constrain volatile mass fluxes, instead of the precise PT location of potentially thousands of phase reactions and relations.

`Rcrust` was used to retain and extract fluids during metamorphism. A retention-to-extraction ratio equal to zero does not signify that all volatiles are extracted, but that all free fluids are extracted. The retention of much free fluid at depth is unstable and geophysically implausible, and we find that even the "*EM-CI*, Retain 5 wt. %" model allows for excessive free fluid at depth (Fig. S9 and S11), which would be expelled in geologically short timescales under compaction as occurs on Earth (e.g. Warner, 2004). For context, the majority of water in Earth's lower crust and mantle is in minerals, not in free fluids. Minerals may have a high volatile retention capacity (as seen in the phase abundance plots in Figures S12 and S13). Retention of free fluids causes much of the silicate layer to have a density that is too low for Europa ($<$ 3000 kg/m^3; Fig. S11); a present-day hydrated silicate interior for Europa is implausible given gravity and density measurements, and thermal history implied by a metallic core (Anderson et al., 1998; Sohl et al., 2002; Schubert et al., 2009; Kuskov & Kronrod, 2005; Vance et al., 2018).

`CHIM-XPT`

For the ocean column compositions, we do not use the DEW because it is not calibrated for low pressures (from the seafloor to the surface). Instead we use the `CHIM-XPT` model and SOLTHERM database (Reed, 1998, see main text). We equilibrate (respeciate) the extracted metamorphic fluids at the seafloor at 273.16 K and do not suppress minerals, gases or species on the basis of kinetic inhibition at low temperature (e.g., dolomite, reduced carbon species, etc.), since the fluids were produced and extracted at high temperature during metamorphism. `CHIM-XPT` is a multiphase equilibrium mass action code, used here to compute the speciation of fluids from 200 MPa (assumed maximum pressure at the seafloor) to 0.1 MPa (the surface of a hypothetical ice-free ocean), including mineral precipitation and gas boiling. These are tasks for which `CHIM-XPT` is particularly well-suited, given its validation against samples obtained in the same pressure range, including borehole and petrologic data in hydrothermal/geothermal systems (Freedman et al., 2009; Fowler et al., 2019), seafloor alteration by diverse fluid compositions (Palandri & Reed, 2004) and experiments simulating CO_2 injection into natural and synthetic samples (Verba et al., 2014). We caution that as with other geochemistry/thermodynamic equilibrium programs, `CHIM-XPT` results may be non-unique. For example, `CHIM-XPT` predicts that any of various mineral-water reactions would yield the serpentine mineral assemblage observed in altered ophiolites (Sonzogni et al., 2017).

Table S4: `Perple_X` solution models used

Table 4. Solution models used in the `Perple_X` thermodynamic phase equilibrium calculations using the DEW17HP622ver_elements thermodynamic data. For the core, we use the SE15ver (Saxena & Eriksson, 2015) data instead.

Solution model	Type	Source
Atg(PN)	Antigorite	Padrón-Navarta et al. (2013)
Bi(HGP)	Biotite	Holland et al. (2018)
Chl(HP)	Chlorite	Holland et al. (1998)
COH-Fluid+	CO_2-CH_4-H_2-CO-H_2O-H_2S-SO_2 fluid with non-linear subdivisions	Connolly and Galvez (2018)
Cpx(HGP)	Clinopyroxene	Holland et al. (2018)
Do(HP)	Dolomite-ankerite	Holland et al. (1998)
Gt(HGP)	Garnet	Holland et al. (2018)
M(HP)	Magnesite-siderite-rhodochrosite	Holland et al. (1998)
melt(HGP)	Generic silicate melt	Holland et al. (2018)
Mica(CF)	Fe-Mg-K-Na mica	Chatterjee and Froese (1975); Holland et al. (1998)
O(HGP)	Olivine	Holland et al. (2018)
Omph(GHP)	Omphacite	Green, Holland, and Powell (2007)
Opx(HGP)	Orthopyroxene	Holland et al. (2018)
Pl(JH)	Plagioclase	Jennings, Holland, Shorttle, Maclennan, and Gibson (2016)
Pu	Pumpellyite	DEW17HP622ver_elements
Sp(HGP)	Spinel	Holland et al. (2018)
Stlp	Stilpnpmelane	DEW17HP622ver_elements
T	Talc	DEW17HP622ver_elements

Text S3: Core composition

Europa's core has variously been approximated as a body composed entirely of Fe (Anderson et al., 1998; Vance et al., 2018), stoichiometric FeS (Kuskov & Kronrod, 2005), 90 wt. % Fe + 10 wt. % S (Kuskov & Kronrod, 2005), or a Fe-SeS eutectic composition (Anderson et al., 1998). However, experimental work has suggested that the core of Europa may be pyrrhotite-rich (Scott et al., 2002). In addition, the pyrrhotite group ($Fe_{(0.8–1)}S$), including its stoichiometric endmember troilite (FeS), is the most abundant Fe-sulfide in chondrite meteorites (e.g. Bland et al., 2004; Singerling & Brearley, 2018). Therefore, we assume that prograde metamorphism proceeded at least up to the Fe-SeS eutectic temperature in order for core formation to proceed. Additionally, pyrrhotite polymorphs are the thermodynamically stable sulfide phases up to the Fe-SeS eutectic temperature under the range of pressures of Europa's interior (Figures S2–S3). Since core formation occurs at higher temperatures than volatile-releasing metamorphic reactions (see Main Text §2.2), core formation does not sequester volatiles that would build the ocean.

The Fe ± S melt phase contains 24–32 mass % sulfur at the < 8 GPa range of pressures within Europa (Figures S2–S3). We do not find a compelling reason on the basis of cosmochemistry to disallow other light elements (oxygen, silicon, carbon, hydrogen) from partitioning into the core, in addition to or in substitution of sulfur, as has been postulated for Earth and Mars (e.g., Wood et al., 2013; Li & Fei, 2014; Badro et al., 2015; Steenstra & van Westrenen, 2018). However, the Fe–S system is simple and well-studied (e.g., Walder & Pelton, 2005) and can provide an initial approximation for an expected core composition, mass and density, until a future mission can constrain the deep interior composition of Europa from its seismic properties and improved gravity data.

Figure S2: Pseudosections of Fe ± S for core formation

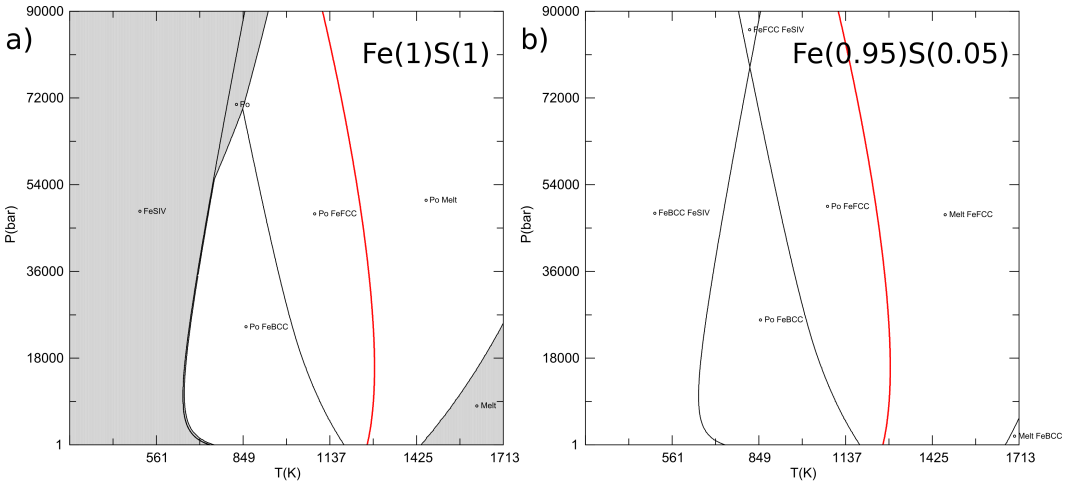

Figure 2. Pseudeosection diagrams of a) stoichiometric FeS, and b) $Fe_{0.95}S_{0.05}$ calculated with `Perple_X` 6.8.7. and thermodynamic constraints from Saxena and Eriksson (2015). Red curve is the Fe–S solidus, also the location of the Fe-SeS eutectic temperature. We assume that prograde metamorphism proceeded at least up to the Fe-SeS eutectic temperature (also the location of the solidus of $Fe_{(1,0.5]}$–$S_{(0,0.5]}$) in order to lead to the formation of a Fe-rich core, since Fe-SeS melt pockets must percolate through the body to coalesce separately from silicates. Pyrrhotite polymorphs are the thermodynamically stable sulfide phases up to the Fe-SeS eutectic temperature under the range of pressures of Europa's interior. FeSIV = polymorph IV of stoichiometric FeS, Po = pyrrhotite, FeBCC = body-centered cubic allotrope of Fe, FeFCC = face-centered cubic allotrope of Fe.

Figure S3: Quantification of Fe ± S melt for core formation

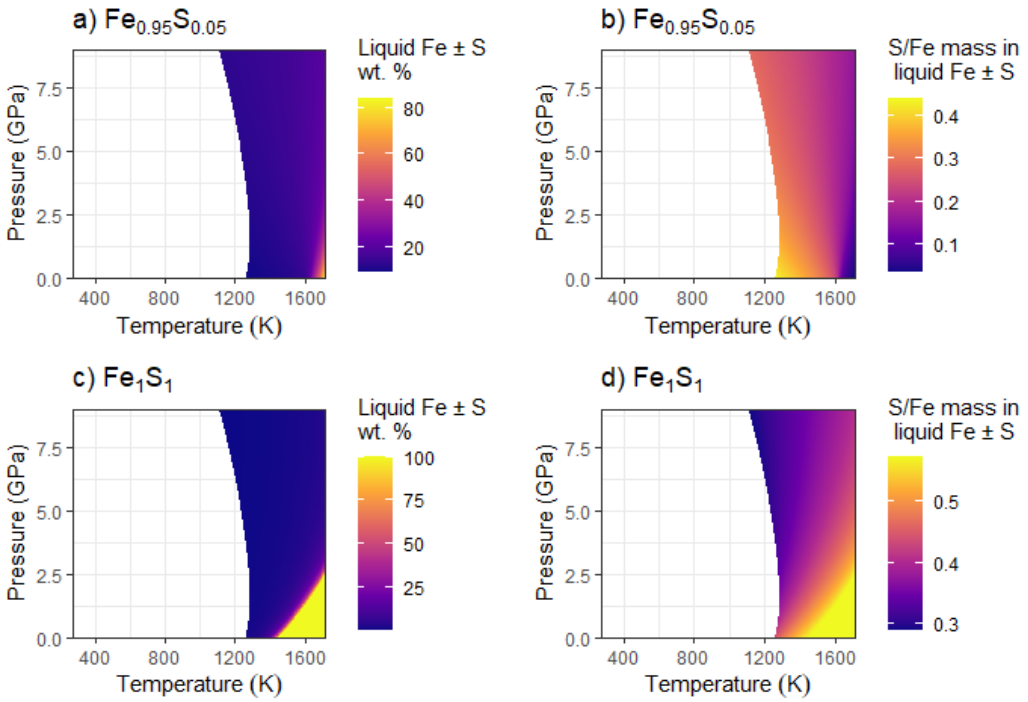

Figure 3. Weight % of Fe ± S melt, and mass fraction of sulfur in Fe ± S melt at and above the Fe-SeS eutectic temperature for pressure conditions relevant to Europa's interior, calculated with `Perple_X` 6.8.7. and thermodynamic constraints from Saxena and Eriksson (2015). We find that Fe ± S melt phase contains 24–32 mass % sulfur at the Fe-SeS eutectic at range of pressures within Europa. a) and b) bulk composition = $Fe_{0.95}S_{0.05}$; c) and d) bulk composition = stoichiometric FeS.

Text S4: Modifications to `PlanetProfile`

`PlanetProfile` calculations were made using the newly computed mantle and core properties from this work. Interior properties shown in Figure S11 are for the CM model, assuming a seawater composition (36.165 g/kg), with temperatures at the bottom of the icy lithosphere set at {270.8,268.2} K for ice thicknesses of {5,30} km. Corresponding core and mantle radii are 450 km and 1410 km, and output moments of inertia (MoI) C/MR^2 are {0.3455,0.3457} for the applied precision of the model. Geotherms in the solid interior are computed for the assumption of 100 GW heat at the seafloor.

Text S5: Additional results of the coupled prograde metamorphism-plus-fluid extraction models

Here we describe additional details about the results of the prograde metamorphism models leading to fluid production and extraction. Figure S6 summarizes the absolute mass of elements delivered into the hydrosphere by prograde metamorphism. Table S5 puts those results into context relative to the accreted composition and mass of Europa. Figures S7–S10 show the composition and source of the fluid extracted from the deep interior at different pressures with increasing temperature for all the *EM-CI* models and the *MC-Scale* model, equivalent to the *EM-CM* model shown in the main text.

The colored areas in the solvent plots (Figs. S7–S10) show regions in pressure-temperature space where that particular solvent (whether extracted or retained) is stable, and what the concentration of that solvent is, in units of moles of the specific solvent per kilogram of total solvents. The element concentration plots show the regions in pressure-temperature space where particular elements (existing in solvents and solutes) are extracted, in weight % of the total fluid extracted. In certain regions of pressure-temperature space, fluid (solvents and solutes) may be thermodynamically stable but may not end up being extracted, i.e., fluids are near their saturation point. For example, the plot for water as a solvent in Figure S9 (*EM-CI*, R/E = 5 wt. %) shows water to be present in a wider pressure and temperature space than the combined extracted H and extracted O plots do, or even the "mass % extracted" plot. This is because of the imposed retention-to-extraction rule: only free fluids that exceed 5 wt. % of the total assemblage are extracted. In other models where no fluid retention rules are imposed, minimal amounts of free fluids may exist at the end of a heating step, but be resorbed into the mineral phases when the model thermodynamically equilibrates the phase assemblage again.

Prograde metamorphic heating paths and how to read them: a walk-through using results

Here we relate further details about the deep interior's mineralogical composition post-differentiation. The effect of prograde metamorphism and associated fluid extraction on the density of the interior is shown in Figure S11. Figures S12 and S13 show the mineralogy at 500 MPa and 3 GPa with increasing temperature respectively, for the *EM-CI* R/E = 0, *EM-CM* R/E = 0, and *MC-Scale* R/E = 0 models.

Compared to *MC-Scale*, fluids begin to be extracted at lower temperature (<400 K) in the *EM-CI* and *EM-CM* models. This comes about because the initial bulk *EM-CI* and *EM-CM* compositions contain excess water that cannot be fully accommodated by hydrous minerals. Most fluid in the thermal evolution of *MC-Scale* is extracted during the decomposition of carbonates (magnesite and dolomite) and phyllosilicates (antigorite and chlorite), leading to high masses of Al and Mg extracted together with water and CO_2 (Figs. S6 & S10). Additionally, large concentrations of Na (up to 10 wt. % of the fluid phase) and Si are exsolved at specific pressures and temperatures (Fig. S10) as Na-bearing clinopyroxene is transformed to Na-free clinopyroxene + olivine at 550 to 1050 K (Fig. S12 & S13).

We describe one of the heating paths here to walk the reader through the results, including the mineralogical changes, fluids generated and extracted, and the effects of fluid extraction on Europa's density. We focus on the *EM-CM* R/E = 0 model as an example. Firstly, Figure 11g shows that the heating of the *EM-CM* body releases free fluids at all depths from the surface of Europa to the center, starting from 293 K. Higher amounts of fluids extracted denote points in P-T space where a volatile-bearing phase begins to transform to a volatile-free phase. The overall results of heating up to

the Fe-SeS solidus (left to right on Fig. 11g) has the overall effect of increasing density as volatiles are released and extracted (Fig. 11i).

At the start (273.15 K) of an isobaric heating path at 500 MPa, the most abundant phase in the *EM-CM* body (Fig. 12b) is antigorite ($Mg_3Si_2O_5(OH)_4$). Other stable volatile-bearing phases are calcite ($CaCO_3$), Mg-chlorite/clinochlore ($Mg_5Al_2Si_3O_{10}(OH)_8$), greenalite ($(Fe^{II},Fe^{III})_3Si_2O_5(OH)_4$), dolomite ($CaMg(CO_3)_2$), goethite ($FeO(OH)$), pyrite ($FeS_2$), and graphite (C). In addition, free fluid is thermodynamically stable, before fluid extraction is allowed to proceed. By $\sim$ 340 K, goethite has transformed into spinel/magnetite (Fe_3O_4), releasing water; antigorite abundance increases at the expense of greenalite, and calcite is transformed into dolomite by $\sim$ 400 K. At $\sim$ 510 K, pyrite transforms to troilite, releasing sulfur ($FeS_2 \longrightarrow FeS + S$), and talc forms at the expense of antigorite. At 780–840 K, antigorite, dolomite, magnesite ($MgCO_3$) and talc ($Mg_3Si_4O_{10}(OH)_2$) destabilize completely in a series of reactions yielding clinochlore, clinoenstatite ($MgSiO_3$), forsterite (Mg_2SiO_4), H_2O and CO_2:

$$\underset{\text{antigorite}}{3\,Mg_3Si_2O_5(OH)_4} \longrightarrow \underset{\text{forsterite}}{Mg_2SiO_4} + \underset{\text{(clino)enstatite}}{MgSiO_3} + \underset{\text{Al-free chlorite}}{Mg_6Si_4O_{10}(OH)_8} + 2\,H_2O \tag{2}$$

$$\underset{\text{antigorite}}{Mg_3Si_2O_5(OH)_4} + \underset{\text{magnesite}}{MgCO_3} \longrightarrow 2\,\underset{\text{forsterite}}{Mg_2SiO_4} + 2\,H_2O + CO_2 \tag{3}$$

$$\underset{\text{antigorite}}{Mg_3Si_2O_5(OH)_4} + \underset{\text{talc}}{Mg_3Si_4O_{10}(OH)_2} \longrightarrow 6\,\underset{\text{enstatite}}{MgSiO_3} + 3\,H_2O \tag{4}$$

Finally, at 880–900 K, clinochlore reacts with clinoenstatite to yield forsterite, the amphibole pargasite ($NaCa_2(Mg_4Al)(Si_6Al_2)O_{22}(OH)_2$), and fluid. A small amount of water remains in pargasite, until it destabilizes to form nepheline ($NaAlSiO_4$) + clinopyroxene at $\sim$ 1180 K.

The stable phase assemblage evolves differently at higher pressure. Taking the 3 GPa isobaric heating path as an example (Fig. 13b), the low temperature phases of the *EM-CM* body consist mainly of goethite, lizardite ($Mg_3Si_2O_5(OH)_4$) and talc, and minor amounts of lawsonite ($CaAl_2Si_2O_7(OH)_2H_2O$), clinoenstatite, pyrite and pumpellyite ($Ca_4MgAl_5Si_6O_{21}(OH)_7$). The mineral hosts of carbon are diamond, and to a lesser extent, magnesite. At $\sim$ 420 K, antigorite replaces lizardite, and chlorite replaces lawsonite. Goethite destabilizes at $\sim$ 540 K, yielding spinel/magnetite and water. Pyrite transforms to troilite at $\sim$ 700 K, releasing sulfur. Talc destabilizes completely at $\sim$ 720 K to enstatite, and at $\sim$ 780–800 K, antigorite, magnetite and diamond transform to graphite, magnesite and olivine, releasing water. At $\sim$ 930 K, clinochlore dehydrates to garnet/pyrope:

$$\underset{\text{clinochlore}}{Mg_5Al_2Si_3O_{10}(OH)_8} + \underset{\text{(clino)enstatite}}{2\,MgSiO_3} \longrightarrow 2\,\underset{\text{forsterite}}{Mg_2SiO_4} + \underset{\text{pyrope}}{Mg_3Al_2Si_3O_{12}} + 4\,H_2O \tag{5}$$

Finally, a carbon-rich fluid is released at $\sim$ 1150 K, when most magnesite destabilizes:

$$\underset{\text{enstatite}}{MgSiO_3} + \underset{\text{magnesite}}{MgCO_3} \longrightarrow \underset{\text{forsterite}}{Mg_2SiO_4} + CO_2 \tag{6}$$

Effect of redox state on fluids extracted during prograde metamorphism

Contrary to preventing carbon from being released from the interior, the reduced conditions (*EM-CI, FMQ-2*, R/E = 0) prevent the stabilization of carbonates that would act as a carbon sink; carbon is released at low temperatures as CH_4 (Fig. S4). At high temperatures where graphite would be stable, no carbon remains to form it. Hence, reduced conditions actually promote the extraction of carbon during the early stages of Europa's differentiation. Figure S5 shows the composition of the ocean column, including precipitating minerals and exsolving gases. The total mass of CH_4 plus H_2 released from the interior and ocean (CO_2 is unstable) amounts to $\sim 10^{22}$ kg, equivalent to a 356 MPa CH_4 + H_2 volatile envelope. The liquid water ocean then amounts to $\sim 7.8 \times 10^{21}$ kg, about 0.16 wt. % of Europa's total mass. Thus, reduced conditions for the building material of Europa were unlikely because they yield a small ocean, inconsistent with observations.

Effect of fluid retention on extracted fluid compositions

Retaining exsolved fluids between temperature steps affects the pattern of volatile release and extraction by spreading the range at which fluids are extracted to higher temperatures at all pressures. However, lower total masses are extracted (Figs. S6 and S7–S9). For example, Ca + Cl are extracted at higher temperatures and lower pressures when fluid is retained (R/E = 0.1; Fig. S8) than when all exsolved fluids are extracted (R/E = 0; Fig. S7). The exsolution and extraction of sulfur are also shifted to higher temperatures if fluid is retained (Fig. S8). The effect is subtle for the R/E = 0.1 and clearer for the flat retention of 5 wt. % fluid (Figs. S8 and S8). Fluid retention significantly decreases the amount of dissolved Si (as aqueous SiO_2, $NaHSiO_3$ and $Mg(HSiO_3)_2$); Na (as aqueous NaCl, $NaHSiO_3$ and Na^+), K (as aqueous KCl, KOH and K^+), Mg (as dissolved Mg^{2+}, $MgCl_2$, $Mg(HSiO_3)_2$, $MgOH^+$ and $MgCO_3$), and Al (as $AlO_2{}^-$) (Fig. S4) since these are transferred from the retained fluid into rock-forming minerals in subsequent heating steps (see also Figs. S12–S13 and main text Equations 2–8). The opposite holds true for iron: retaining fluids causes Fe to increase in solution, where it is found as aqueous $FeCl_2$, $FeCl_3$, Fe^{2+} and $FeCl^+$ (Fig. S6, and S7–S8).

Chlorine and sulfur extracted into the hydrosphere

While the mass of chlorine extracted relative to the mass of chlorine in all bulk accreted compositions far exceeds the mass of sulfur extracted relative to the mass of initially accreted sulfur (mass chlorine extracted/mass chlorine accreted $\gg$ mass sulfur extracted/mass sulfur accreted), in all models the absolute mass of sulfur in the extracted ocean exceeds the mass of extracted chlorine by an order of magnitude (Table S5).

Figure S4: Extracted fluid composition for *EM-CI*, FMQ-2, R/E = 0

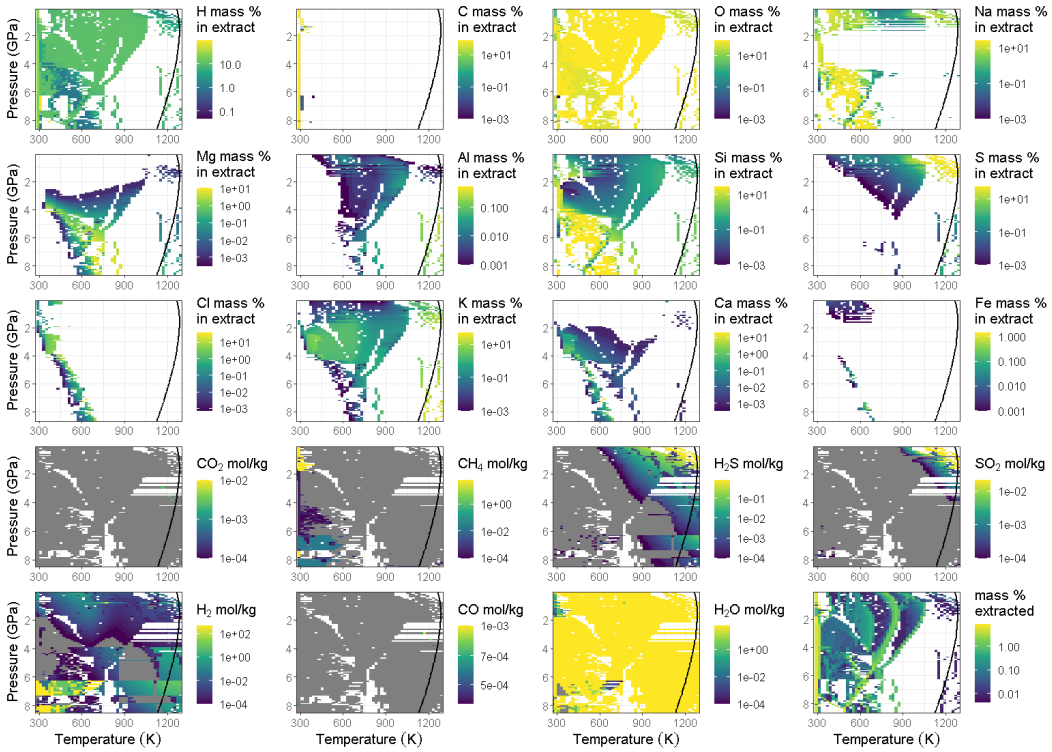

Figure 4. Composition of the fluid extracted from the deep interior at different pressures with increasing temperature for the *EM-CI, FMQ-2* R/E = 0 model. The solid curve shows the Fe-SeS eutectic temperature. Integrating up to the eutectic yields the total amounts exsolved from the deep interior. Blank areas signify that no fluids containing the specific element shown in the plot were extracted at those pressures and temperatures. Rows 1–3: elemental abundance of the extracted fluid (solvents and solutes). Rows 4–5: molecular solvent moles per kilogram of extracted fluid. Grey areas in the solvent plots signify that fluids were extracted at those pressures and temperatures, but did not contain the specific solvent shown in the plot. Bottom-right plot: total extracted mass.

Figure S5: Ocean column composition for *EM-CI* FMQ-2, R/E = 0

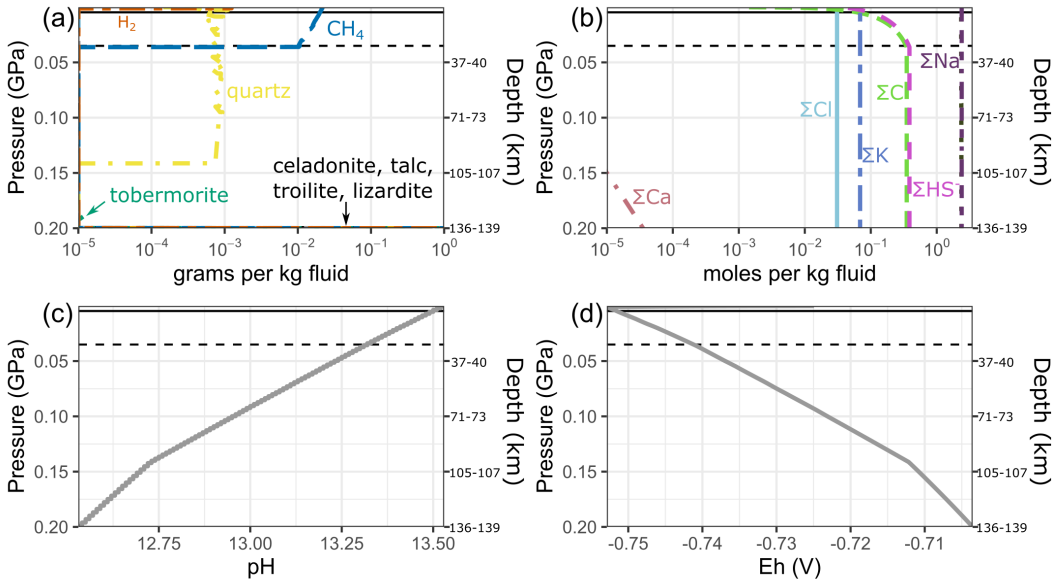

Figure 5. Ocean column compositions from the seafloor to the surface, for *EM-CI, FMQ-2*, R/E = 0. Solid and horizontal lines show the pressure at the base of a current 5 km and 30 km ice shell respectively (see Main Text §3.3). a) Minerals precipitated and gases exsolved with decreasing depth in the water column. b) Total dissolved components in the water column. Dissolved components shown here are the sum of those particular components distributed among all species in solution. For example, component ΣC represents the sum of carbon in aqueous HCO_3^-, CH_4, CO_2, and organics, among other species. Concentrations $< 10^{-5}$ mol/kg not shown. c) pH, and d) redox potential of the ocean column.

Figure S6: Absolute mass of elements extracted for all prograde metamorphism models

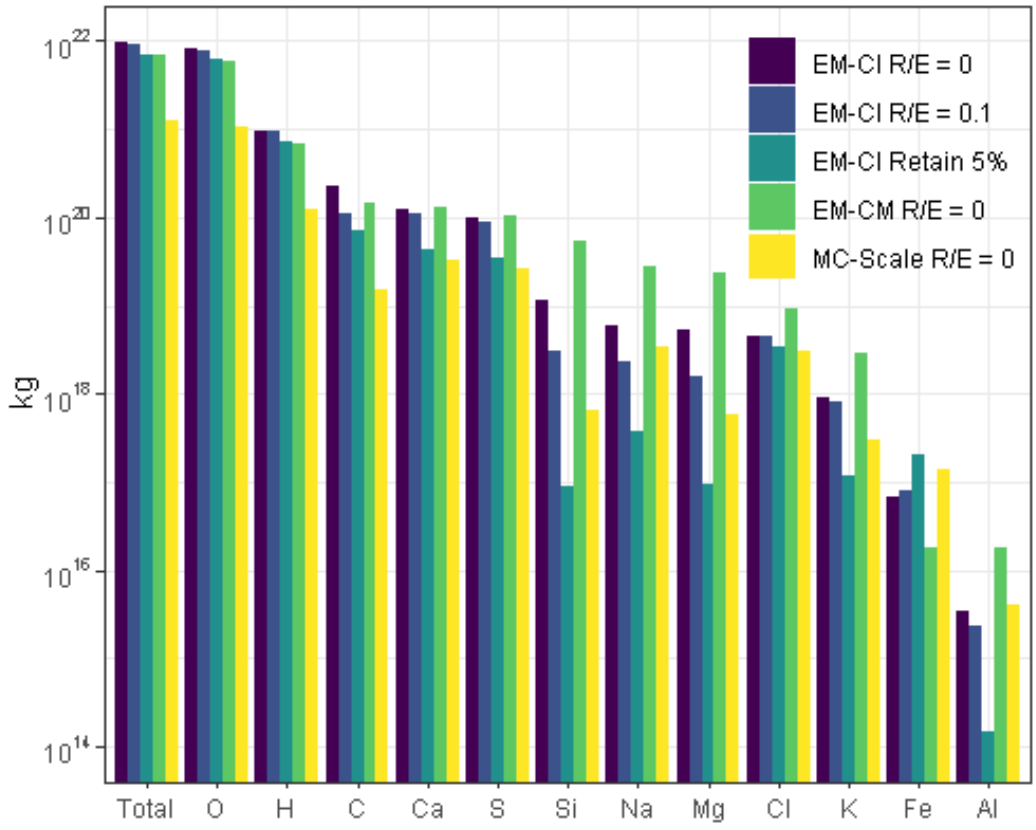

Figure 6. Absolute mass of elements in the extracted hydrosphere reservoir during prograde metamorphism of the deep interior up to the stoichiometric Fe-SeS eutectic temperature at all depths.

Table S5: Mass and elemental composition of the extracted bulk fluid in context

Table 5. Mass and elemental composition of the extracted bulk fluid (unequilibrated with itself) for each model, in context with accreted elements and Europa's mass. *EM-CI* = endmember CI initial bulk composition, *EM-CM* = endmember CM initial bulk composition *MC-Scale* = Monte Carlo scaled initial composition, R/E = retained-to-extracted fluid mass ratio, M_{Ext} = mass extracted, M_{Eur} = mass of Europa, M_{Acc} = bulk mass initially accreted for each element.

	EM-CI						*EM-CM*		*MC-Scale*	
	R/E=0		R/E=1:10		Extract all at >5 wt. %		R/E=0		R/E=0	
	M_{Ext}/M_{Eur} %	M_{Ext}/M_{Acc} %	M_{Ext}/M_{Eur} %	M_{Ext}/M_{Acc} %	M_{Ext}/M_{Eur} %	M_{Ext}/M_{Acc} %	M_{Ext}/M_{Eur} %	M_{Ext}/M_{Acc} %	M_{Ext}/M_{Eur} %	M_{Ext}/M_{Acc} %
H	2.00	99.48	1.97	97.58	1.54	76.55	1.39	97.22	0.26	67.36
C	0.46	12.99	0.23	6.58	0.15	4.10	0.30	13.25	0.03	3.57
O	17.35	36.97	16.45	35.05	12.76	27.18	12.15	27.53	2.25	5.72
Na	0.01	2.45	<0.01	0.95	<0.01	0.15	0.06	14.21	0.01	2.01
Mg	0.01	0.11	<0.01	0.03	<0.01	<0.01	0.05	0.41	<0.01	0.01
Al	<0.01	<0.01	<0.01	<0.01	<0.01	<0.01	<0.01	<0.01	<0.01	<0.01
Si	0.02	0.22	0.01	0.06	<0.01	<0.01	0.11	0.87	<0.01	0.01
S	0.21	3.77	0.18	3.36	0.07	1.29	0.22	8.01	0.06	2.59
Cl	0.01	81.16	0.01	79.28	0.01	61.15	0.02	97.28	0.01	90.44
K	<0.01	3.32	<0.01	3.04	<0.01	0.43	0.01	16.17	<0.01	93.48
Ca	0.26	27.08	0.23	24.43	0.09	9.54	0.28	21.22	0.07	4.23
Fe	<0.01	<0.01	<0.01	<0.01	<0.01	<0.01	<0.01	<0.01	<0.01	<0.01
Total	20.34	20.34	19.09	19.09	14.61	14.61	14.58	14.58	2.69	2.69

Figure S7: Extracted fluid composition for *EM-CI* R/E = 0

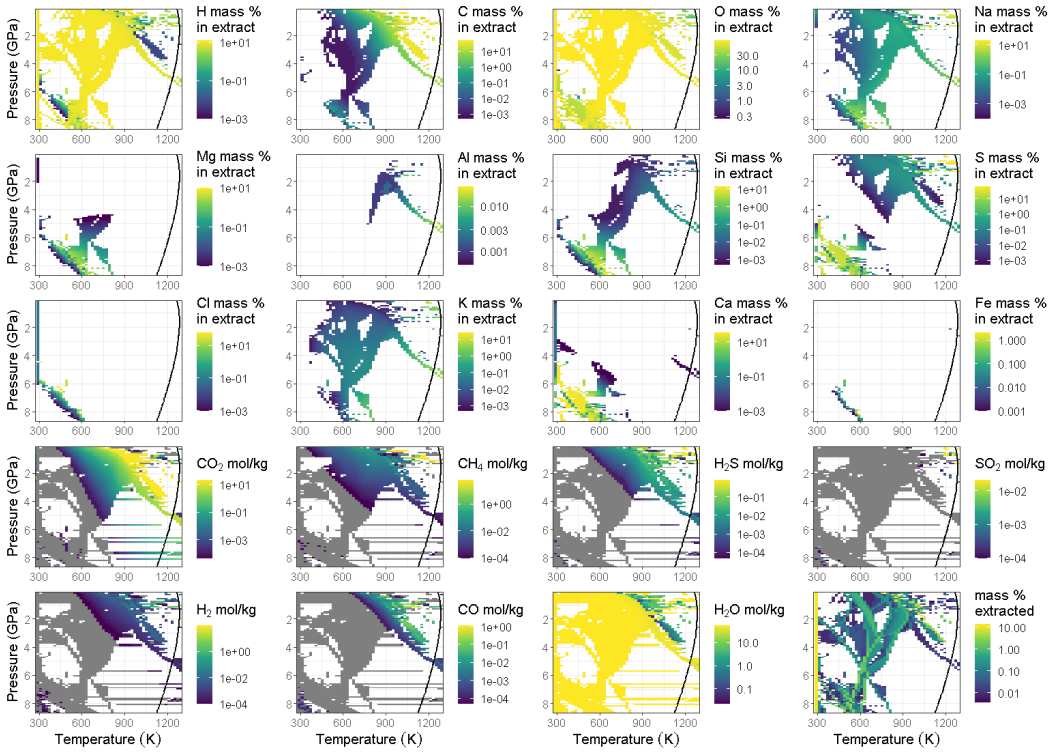

Figure 7. Composition of the fluid extracted from the deep interior at different pressures with increasing temperature for the *EM-CI* R/E = 0 model. The solid curve shows the Fe-SeS eutectic temperature. Integrating up to the eutectic yields the total amounts exsolved from the deep interior. Blank areas signify that no fluids containing the specific element shown in the plot were extracted at those pressures and temperatures. Rows 1–3: elemental abundance of the extracted fluid (solvents and solutes). Rows 4–5: molecular solvent moles per kilogram of extracted fluid. Grey areas in the solvent plots signify that fluids were extracted at those pressures and temperatures, but did not contain the specific solvent shown in the plot. Bottom-right plot: total extracted mass.

Figure S8: Extracted fluid composition for *EM-CI* R/E = 0.1

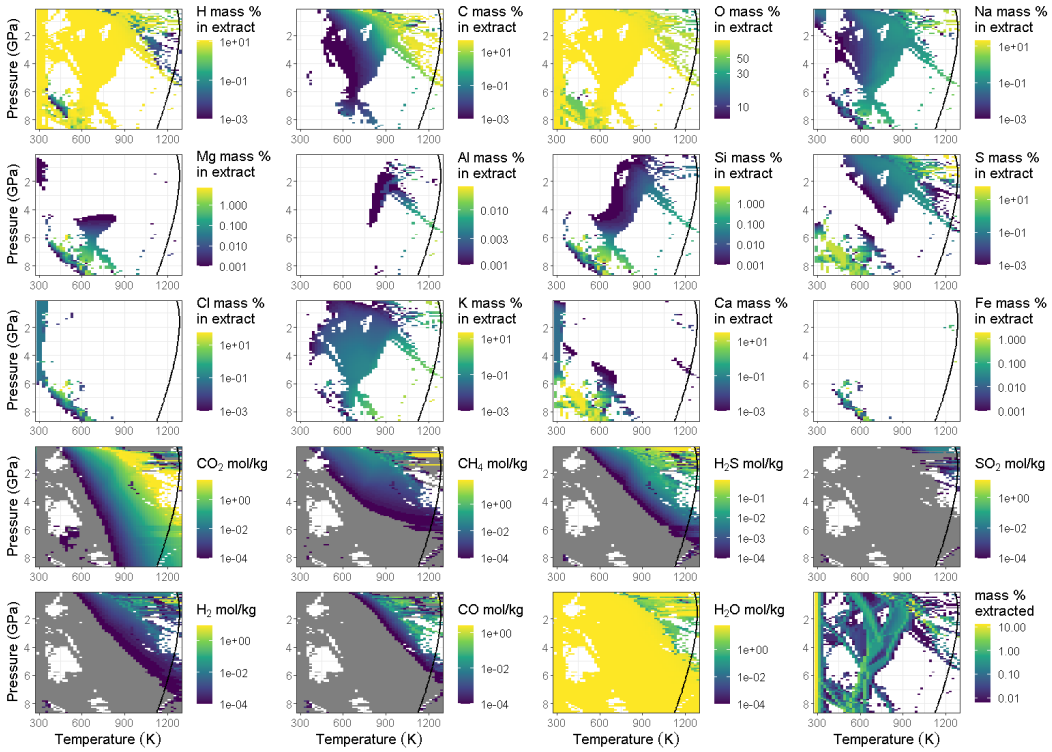

Figure 8. Composition of the fluid extracted from the deep interior at different pressures with increasing temperature for the *EM-CI* R/E = 0.10 model. The solid curve shows the Fe-SeS eutectic temperature. Integrating up to the eutectic yields the total amounts exsolved from the deep interior. Blank areas signify that no fluids containing the specific element shown in the plot were extracted at those pressures and temperatures. Rows 1–3: elemental abundance of the extracted fluid (solvents and solutes). Rows 4–5: molecular solvent moles per kilogram of extracted fluid. Grey areas in the solvent plots signify that fluids were extracted at those pressures and temperatures, but did not contain the specific solvent shown in the plot. Bottom-right plot: total extracted mass.

Figure S9: Extracted fluid composition for *EM-CI*, Retaining 5 wt.% fluid

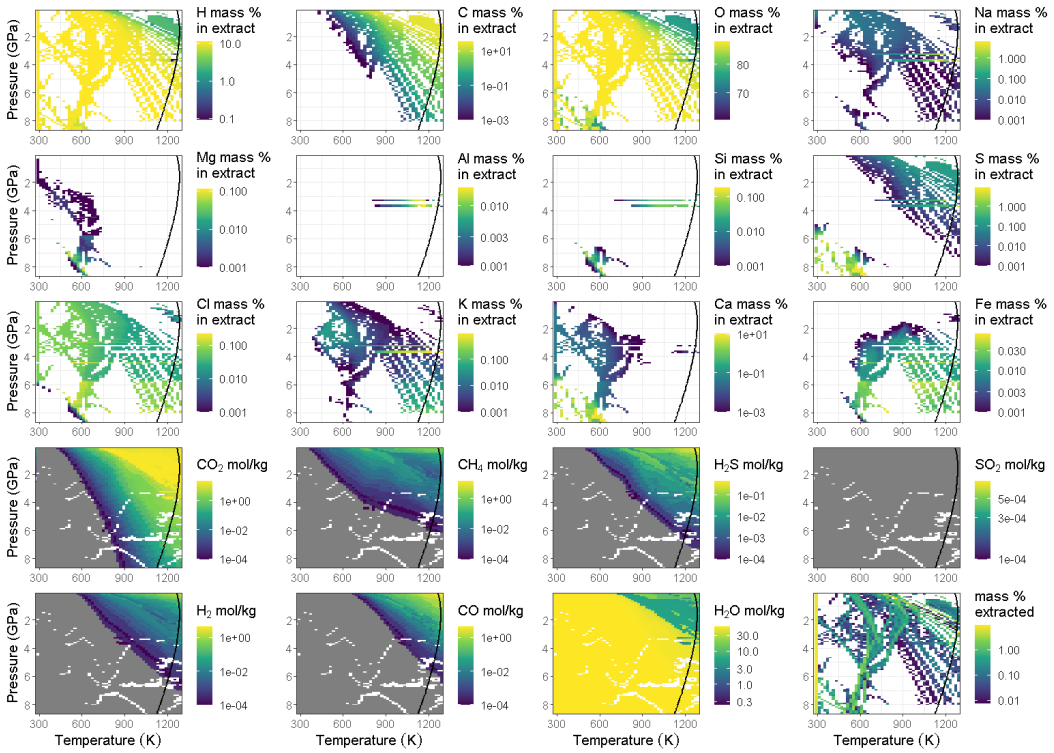

Figure 9. Composition of the fluid extracted from the deep interior at different pressures with increasing temperature for the *EM-CI* Retain 5 wt. % model. The solid curve shows the Fe-SeS eutectic temperature. Integrating up to the eutectic yields the total amounts exsolved from the deep interior. Blank areas signify that no fluids containing the specific element shown in the plot were extracted at those pressures and temperatures. Rows 1–3: elemental abundance of the extracted fluid (solvents and solutes). Rows 4–5: molecular solvent moles per kilogram of extracted fluid. Grey areas in the solvent plots signify that fluids were extracted at those pressures and temperatures, but did not contain the specific solvent shown in the plot. Bottom-right plot: total extracted mass.

Figure S10: Extracted fluid composition for *MC-Scale* R/E = 0

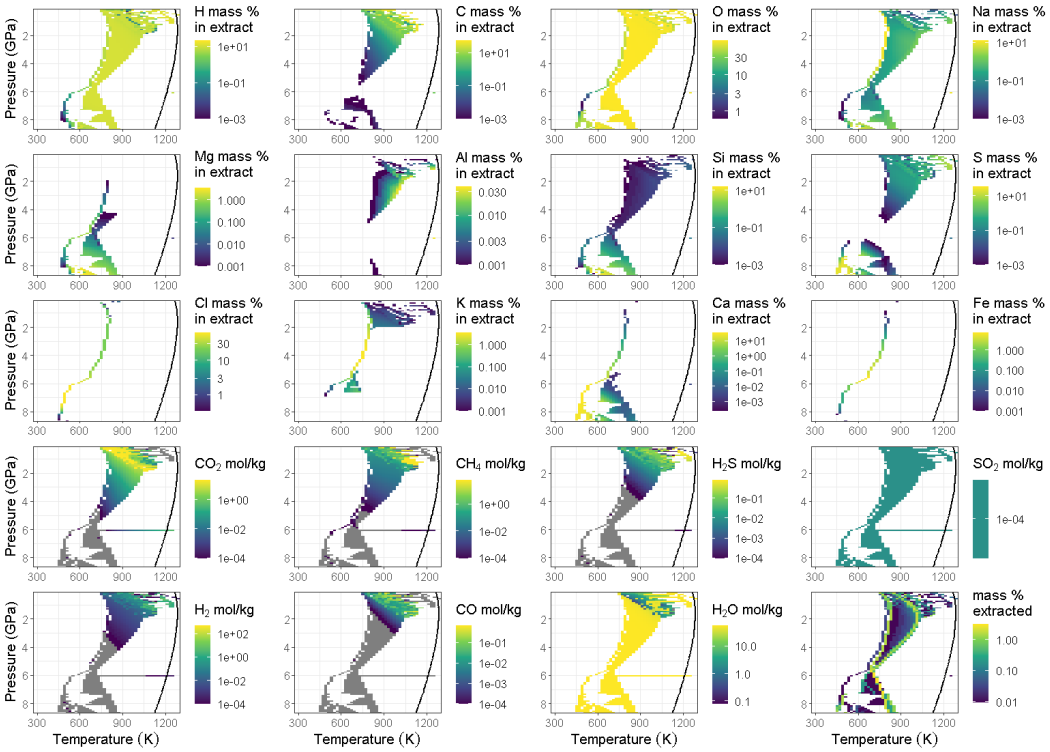

Figure 10. Composition of the fluid extracted from the deep interior at different pressures with increasing temperature for the *MC-Scale* R/E = 0 model. The solid curve shows the Fe-SeS eutectic temperature. Integrating up to the eutectic yields the total amounts exsolved from the deep interior. Blank areas signify that no fluids containing the specific element shown in the plot were extracted at those pressures and temperatures. Rows 1–3: elemental abundance of the extracted fluid (solvents and solutes). Rows 4–5: molecular solvent moles per kilogram of extracted fluid. Grey areas in the solvent plots signify that fluids were extracted at those pressures and temperatures, but did not contain the specific solvent shown in the plot. Bottom-right plot: total extracted mass.

Figure S11: Effect of fluid extraction on the deep interior's density

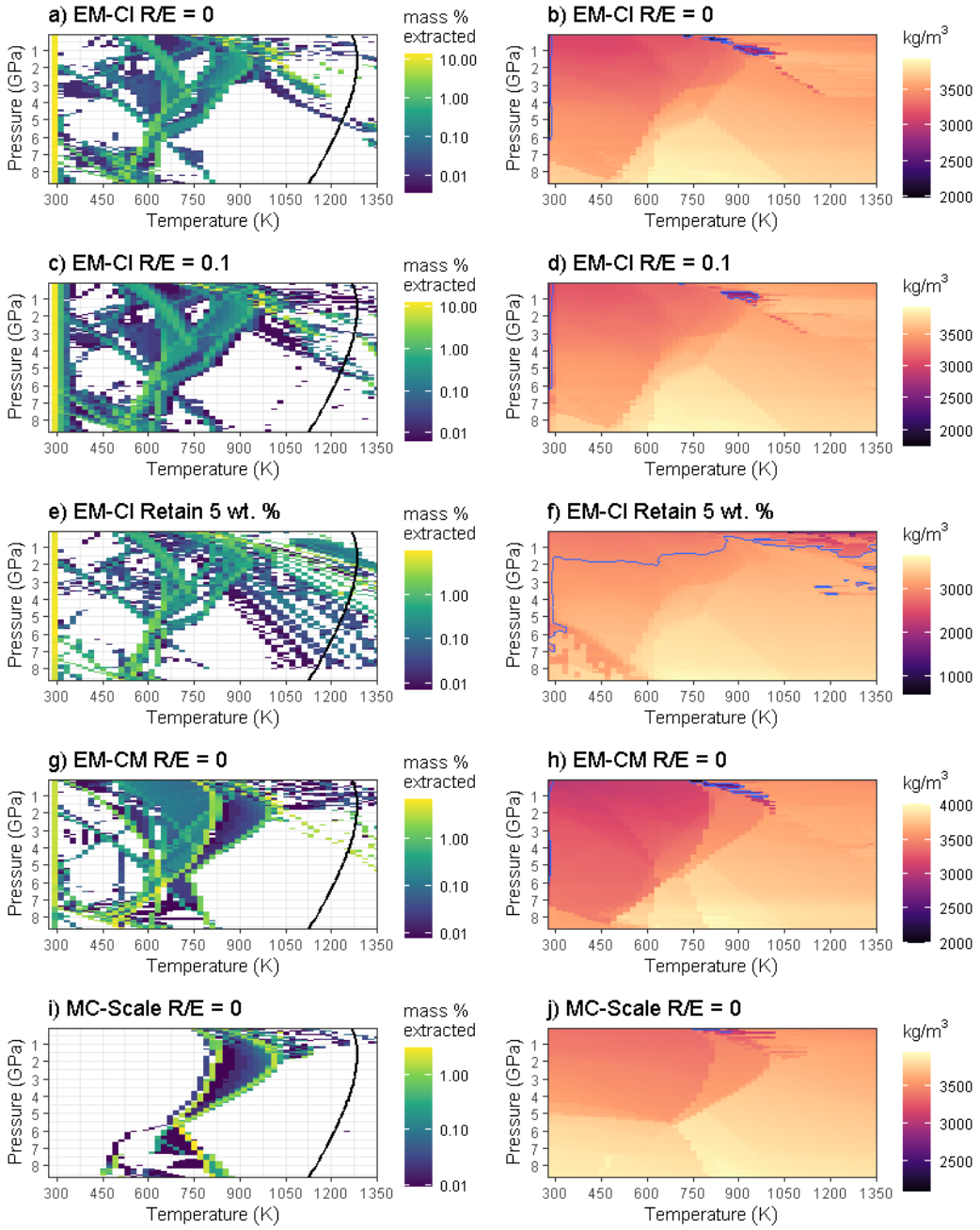

Figure 11. Mass % of fluid transferred into the ocean reservoir during prograde metamorphism of the undifferentiated bulk composition at all depths (left column) and resulting density of the deep interior (right column). Panels in the left column are reproduced from Main Text Figure 2 and Figures S7–S10. The solid black curve represents the Fe-SeS eutetic temperature bracketing the minimum temperature to segregate a Fe ± S core. The blue contour line is an isopycnic line of constant density $\rho = 3000$ kg m^{-3}.

Figure S12: Changing mineralogy at 0.5 GPa in prograde metamorphism/fluid extraction

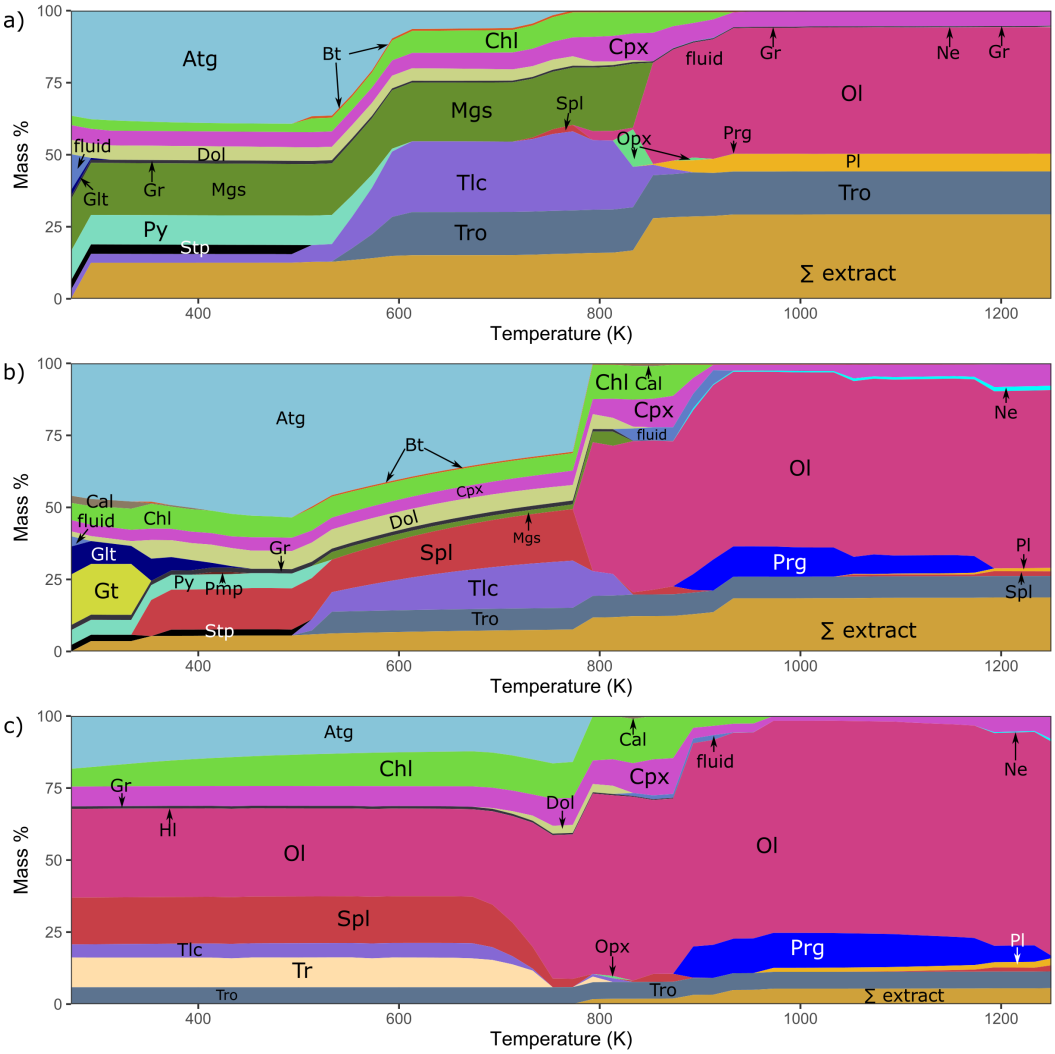

Figure 12. Phase changes and fluid extracted at 500 MPa for a) *EM-CI* R/E = 0, b) *EM-CM* R/E = 0, and c) *MC-Scale* R/E = 0. Phase abbreviations are: Atg = antigorite, Bt = biotite, Chl = chlorite, Cpx = clinopyroxene, Dia = diamond, Dol = dolomite, Glt = greenalite, Gr = graphite, Grt = garnet, Gt = goethite, Hl = halite, Lws = lawsonite, Lz = lizardite, Mgs = magnesite, Ne = nepheline, Ol = olivine, Opx = orthopyroxene, Pl = plagioclase, Pmp = pumpellyite, Prg = pargasite, Py = pyrite, Spl = spinel, Stp = stilpnomelane, Tlc = talc, Tro = troilite. Two immiscible clinopyroxene phases have been binned together. "Σ Extract" is the cumulative extracted fluid with increasing temperature. Free volatiles, i.e., "fluid" can appear in the heating path plots because the phases shown are the result of the sequence: temperature increase + equilibration $\longrightarrow$ fluid extraction $\longrightarrow$ equilibration, i.e., thermodynamic equilibration of the phase assemblage after extraction of free fluid may release fluids again.

Figure S13: Changing mineralogy at 3 GPa in prograde metamorphism/fluid extraction

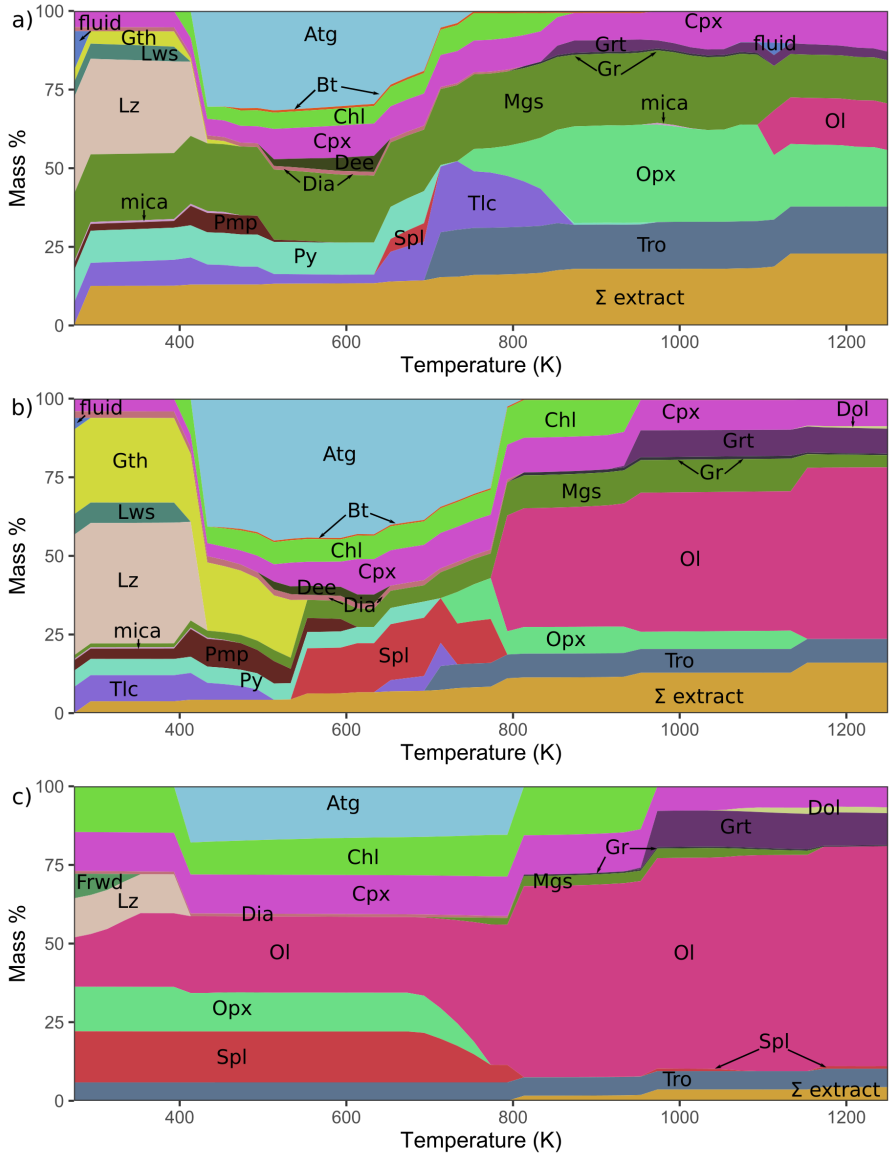

Figure 13. Phase changes and fluid extracted at 3 GPa for a) *EM-CI* R/E = 0, b) *EM-CM* R/E = 0, and c) *MC-Scale* R/E = 0. Phase abbreviations are: Atg = antigorite, Bt = biotite, Chl = chlorite, Cpx = clinopyroxene, Dee = deerite, Dia = diamond, Dol = dolomite, Grt = garnet, Gth = goethite, Gr = graphite, Hl = halite, Lws = lawsonite, Lz = lizardite, Mgs = magnesite, Ol = olivine, Opx = orthopyroxene, Pmp = pumpellyite, Py = pyrite, Spl = spinel, Tlc = talc, Tro = troilite. Two immiscible clinopyroxene phases have been binned together. "Mica" comprises a solid solution of celadonite, ferroceladonite, muscovite and pargasite. "Σ Extract" is the cumulative extracted fluid with increasing temperature. Free volatiles, i.e., "fluid" can appear in the heating path plots because the phases shown are the result of the sequence: temperature increase + equilibration $\longrightarrow$ fluid extraction $\longrightarrow$ equilibration, i.e. thermodynamic equilibration of the phase assemblage after extraction of free fluid may release fluids again.

Text S6: Mechanisms and limits of volatile sequestration and loss to space

The volatile extraction and outgassing considered in this work can be summarized in two consecutive steps: 1) formation of a condensed liquid ocean by the volatiles released from Europa's bulk accreted body on the pathway towards the formation of a Fe-core, and 2) outgassing from the liquid ocean as gases exceed their solubility limit. The outgassing of ~ 27 MPa CO_2 (Main Text Table 1) is an upper limit, based on the assumption that Europa was formed by CI carbonaceous chondrites, which are the most volatile-rich chondrites. Such a scenario leads to an excessively massive hydrosphere (17.8 wt. %), inconsistent with Europa's present-day hydrosphere. We note that for larger, less volatile-rich bodies, the amounts of outgassed primordial volatiles are on the same order of that calculated in this work: 5–25 MPa of H_2O and in excess of 1–5.5 MPa of CO_2 are calculated to have been lost from Mars in the first 12 Myr after accretion (Erkaev et al., 2014; Odert et al., 2018). The mantles and crusts of Mars and other terrestrial bodies would be substantially devolatilized after this primary catastrophic outgassing (Lammer et al., 2013). Secondary, long-term outgassing, is of a significantly lower magnitude (e.g., compare primary outgassing estimates from Erkaev et al. (2014) and Odert et al. (2018), with secondary, nominally volcanic, outgassing in Craddock and Greeley (2009)), and not the focus of this work. We also note that massive primordial atmospheres have been predicted for Triton ($\sim$ 160 MPa pCO_2 Lunine & Nolan, 1992), Ganymede and Callisto (Kuramoto & Matsui, 1994), which have exceedingly thin exospheres at present. In addition, for the CI chondrite and CM chondrite bulk compositions, we predict that the mass of water devolatilized from the interior exceeds Europa's present-day hydrosphere (Figure S6 and Table S5), signifying that the difference between the present hydrosphere mass and the amount exsolved from the interior (1.5×10^{21}–5.5×10^{21} kg H_2O, equivalent to 62–209 MPa pH_2O) would have to have been lost to space.

Sequestration by clathrates

An alternative to loss of CO_2 by the formation of an atmosphere and ultimate loss to space, is the formation of clathrate hydrates. Calculating how a potential clathrate layer at Europa's seafloor affects the thermal properties and lifetime of the ocean is beyond the scope of this work, primarily because it would require a geodynamic simulation accounting for complex feedback (e.g. Kalousová & Sotin, 2020). Nevertheless, we provide further context and summarize what the fate of clathrates would be below, based on known and approximated thermodynamic properties. Whether CO_2 clathrates are stable in Europa's ocean depends on the pressure and temperature, assuming sufficient CO_2 feedstock is present. The thermodynamically favored CO_2 clathrate structure for Europa's ocean would be sI. For large amounts of CO_2 produced here, we calculate sI clathrates with a CO_2/H_2O molar ratio of 0.159 at 273.15 K and equilibrium pressure (1.243 MPa), using the formulation from Sloan and Koh (2008, p. 268). We calculate a clathrate density of 1106 kg/m^3 from:

$$\rho = \frac{N_w M_w + (N_{Lg} M_g \theta_L) + (N_{Sg} M_g \theta_S)}{N_A V_{sI}} \times 1000 \tag{7}$$

where N_w (= 46) is the number of water molecules per sI crystal cell, M_w is the molecular mass of water, N_{Lg} (= 6) and N_{Sg} (= 2) are the number of guest species molecules in the large and small cavities of sI clathrates respectively, M_g is the molecular mass of the clathrate guest species (44 g/mol for CO_2), θ_L (= 0.9808) and θ_S (= 0.7248) are the occupancy fractions for the large and small cavities occupied by the guest species, N_A is Avogadro's number and V_sI is the volume of sI clathrate crystal cells (12×10^{-8} cm^3). Equilibrium pressures for ocean temperatures $\gtrsim$ 277.2 K are

higher than 200 MPa, meaning that CO_2 clathrates would not be stable in Europa's ocean.

We assume that the clathrates sink if their density exceeds the density of the liquid ocean. Using the Pitzer and Sterner (1994) equation of state for H_2O-CO_2 fluids implemented in Perple_X, we calculate that the density of the exsolved ocean composition is comparable to that of seawater, never exceeding the density of the sI CO_2 clathrates (Fig. S14), and therefore the clathrates will tend to sink. This would result in total clathrate thicknesses of 3.4–77 km mantling Europa's seafloor, using the outgassing calculation of 2.65×10^{19}–6.40×10^{20} kg CO_2 (Main Text Table 1) and a seafloor at 140 km beneath the surface (Vance et al., 2018). Previous work by Bouquet, Mousis, Glein, Danger, and Waite (2019) and Prieto-Ballesteros et al. (2005) concur that CO_2 clathrates would sink to the bottom of Europa's seafloor if the composition of Europa's ocean was that of pure or low salinity water. However, equations of state up to 200 MPa adequately describing the density of mixed COHS-fluids including Ca-Na-Mg-K-CO_3-SO_4-Cl salts are currently lacking, and if Europa's ocean became progressively saltier in time, perhaps as a result of progressive freezing of the ice shell, the density of the ocean would exceed the density of the clathrates, and so any clathrates present in the ocean would tend to float towards the surface (Fig. S14). Finally, calculations have shown that magmatism at Europa's seafloor is likely to have occurred over geologic time (Běhounková et al., 2021), so clathrates are unlikely to remain stable at Europa's seafloor for 4.5 Gyr. However: 1) the predicted spatial distribution of dissipation favors magmatism at the poles (Běhounková et al., 2021), so clathrates may remain stable nearer to the equator, and 2) effusive volcanic events may provide silicate rocks at the seafloor that would efficiently react with and sequester aqueous CO_2.

Nevertheless, assuming that the ocean temperature has remained low enough to stabilize clathrates, and that the viscosity of high pressure ice on Ganymede and Titan's seafloors (Choblet et al., 2017; Kalousová & Sotin, 2020) applies to a CO_2 clathrate blanket on Europa's seafloor, then long-term stability of the liquid ocean is still predicted for seafloor mantling layers < 80 km thick and reasonable heat fluxes (> 6 mW/m^2) from the silicate interior into the bottom of the ice or clathrate layer (Kalousová & Sotin, 2020). Melt and heat transport from the bottom of the clathrate layer to the ocean would occur either through hot plume conduits or solid state convection (Choblet et al., 2017; Kalousová & Sotin, 2020). If efficient depletion of CO_2 took place through carbonate formation or clathration, Europa's ocean, like Earth's atmosphere, could have a high N/C ratio. On the other hand, if CO_2 was not substantially lost from the hydrosphere after outgassing, the N/C ratio of the ocean should be low, reflecting periodic resupply from destabilized clathrates, or a primordial ocean composition.

Loss to space

Independent measurements have tentatively detected plumes at Europa (Jia et al., 2018; Roth et al., 2014; Sparks et al., 2016), which provide a plausible process for volatile loss from the ocean. We estimate the mass ejection rate of a representative conic plume as:

$$\frac{m}{dt} = \frac{\rho \pi r^2}{3} \tag{8}$$

assuming a representative mass $m = 10^6$ kg, radius $r = 135$ km and ejection velocity $v = 100$–1000 m s^{-1} (Roth et al., 2014; Sparks et al., 2016). Plume density ρ is obtained from:

$$\rho = \frac{m}{V} \tag{9}$$

where plume volume V is approximated as a cone:

$$V = \frac{\pi r^2 h}{3} \tag{10}$$

with height h = 200 km (Sparks et al., 2016). We estimate an ejection rate of 5×10^2–5×10^3 kg/s, and 7.2×10^{19}–7.2×10^{20} kg H_2O lost over 4.56 Gyr, or about 1.4–24 % Europa's present ocean mass over the lifetime of the solar system. These represent upper limits since the estimation assumes constant plume activity, and in addition, most of the water would return to the surface given ejection velocities lower than the escape velocity of ~ 2.03 km/s.

Gases exceeding their solubility limit in Europa's warmer primordial ocean, however, are much more likely to escape Europa's gravitational pull. Placing precise constraints on the rate of atmospheric escape is not within the scope of this work, but we mention a number of possible mechanisms prevalent in the Jovian system to motivate further study. While infrared spectroscopy has revealed likely CO_2 ice and possible carbonate signatures presently at Europa's surface (Hansen & McCord, 2008; McCord et al., 1999, 1998), these do not appear to be significant compared to the massive early outgassing of CO_2 calculated in this work. Small bodies may lose much of their heavy atmospheric species through early runaway greenhouse-type episodes, i.e., along with the efficient hydrodynamic escape of H and H_2 (e.g. Lammer et al., 2010). The volatile mixture exsolved from the ocean is CO_2-rich ($CO_2/(H_2O + CO_2)$ = 0.997–0.999; Main Text Table 1), which would limit diffusive thermal escape of hydrogen to space by the infrared cooling effect of CO_2. Alternatively, sputtering caused by incident extreme ultraviolet of the young sun and charged particle flux could directly eject atmospheric species. Additionally, neutral molecules can be ionized, picked up by Jupiter's magnetic field and accelerated away by plasma flow, or back towards the primordial atmosphere, where sputtering resumes. This may result in net dissociation of CO_2, decreasing infrared cooling and leading to a large expansion of the thermosphere, further accelerating loss (e.g. Tian et al., 2009). Constraining the long term impact history of Europa is hampered by the young surface age, but impacts that blew away the early atmosphere may also be possible.

Figure S14: Density of CO_2 clathrates in Europa's ocean

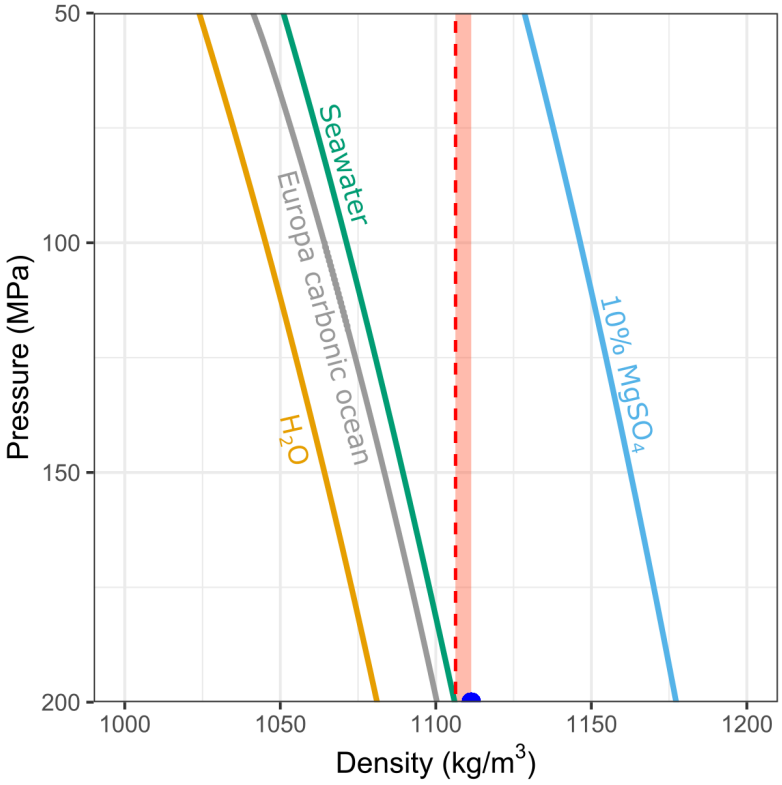

Figure 14. Density of Europa's exsolved carbonic ocean (from the *EM-CI* R/E = 0 model), compared to pure water, seawater and a 10 wt. % $MgSO_4$ ocean, from Vance et al. (2018). The red dashed line shows the density of CO_2 clathrates in Europa's carbonic ocean at 273.15 K, from the equilibrium pressure to seafloor pressures. These clathrates would sink in a carbonic ocean but float in a 10 wt. % $MgSO_4$ ocean.The blue circle shows the equilibrium pressure and density of CO_2 clathrates at 277.23 K. At $>$ 277.23 K, CO_2 clathrates would not be stable in Europa's ocean. The red shaded area shows the range of CO_2 clathrate densities stable in Europa's ocean.

Text S7: Compensating for insufficient volatiles extracted from *MC-Scale* with comets

Prograde metamorphism of the *MC-Scale* model yields an extracted hydrosphere less massive than Europa's present-day hydrosphere (Figs. S6 and S10, and Table S5), so we performed a chemical equilibrium model with `CHIM-XPT` to compensate for the missing ocean mass after metamorphism, by adding cometary material (Table S2). *MC-Scale* produced a 2.63 mass % hydrosphere, so we added 7.31 mass % cometary material to produce a 10 mass % hydrosphere. The resulting ocean composition is reduced, basic, and carbon, silicon, sodium and sulfide-rich (Fig. S15). Graphite, greenalite, pyrite and talc are only stable at the seafloor, while quartz saturates and precipitates throughout the ocean column. Calcite saturates at the bottom, the calcium silicate hydrate tobermorite ($Ca_{0.833}SiO_2(OH)_{1.667}(H_2O)_{0.5}$) saturates in the middle of the ocean, and methane saturates and is exsolved near the top. The mass of precipitates would form a 38.2 km layer at the seafloor while the total mass of exsolved CH_4 would yield a $\sim$ 8 MPa envelope.

Figure S15: Ocean column composition for *MC-Scale* plus cometary material

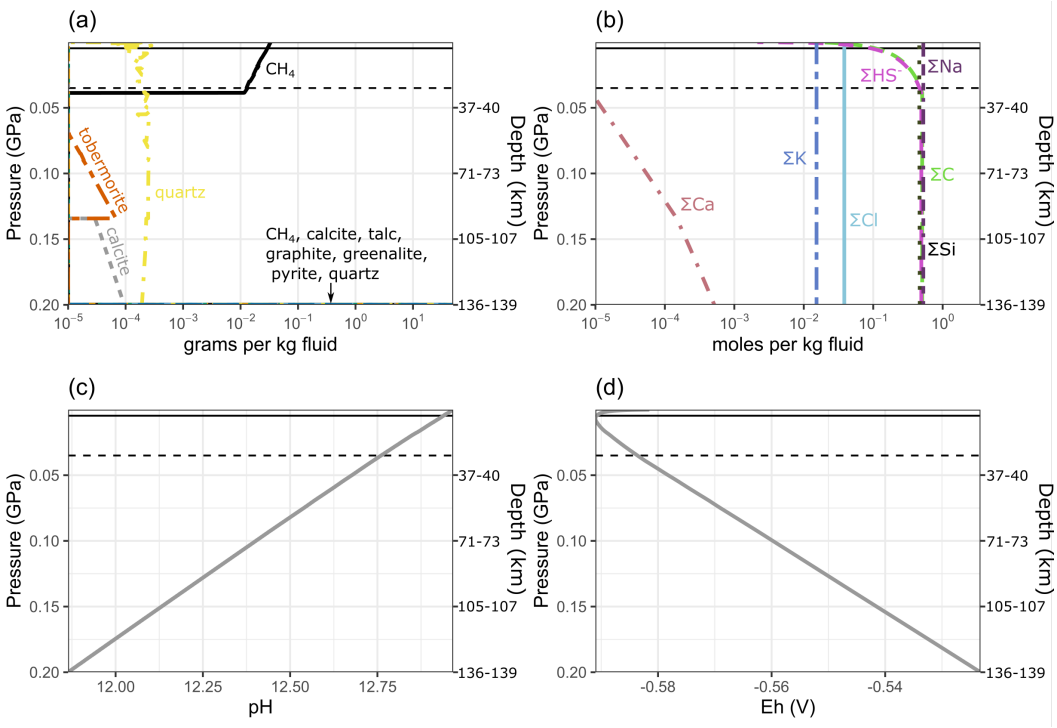

Figure 15. Ocean column compositions from the seafloor to the surface, for *MC-Scale*, R/E = 0, with added cometary material. Solid and horizontal lines show the pressure at the base of a current 5 km and 30 km ice shell respectively (see Main Text §3.3). a) Minerals precipitated and gases exsolved with decreasing depth in the water column. b) Total dissolved components in the water column. Dissolved components shown here are the sum of those particular components distributed among all species in solution. For example, component ΣC represents the sum of carbon in aqueous HCO_3^-, CH_4, CO_2, and organics, among other species. Concentrations $< 10^{-5}$ mol/kg not shown. c) pH, and d) redox potential of the ocean column.

Table S6: Adjusted mass of Europa's hydrosphere for *MC-Scale* plus cometary material

Table 6. Adjusted mass of Europa's hydrosphere after accounting for sediments predicted to precipitate on the seafloor and mass of gases exsolved at low pressure in the ocean column, for the *MC-Scale* model with cometary material added to form a 10 mass % hydrosphere. "Thickness" = globally averaged thickness of the precipitate layer at Europa's seafloor, for a hydrosphere depth of 140 km (see Main Text §3.3). "Adjusted hydrosphere mass" = 10 mass % hydrosphere minus the mass of minerals precipitated and gases exsolved from the water column. M_{Eur} = mass of Europa.

Mineral precipitates	Concentration g/kg fluid	Mass kg
calcite	38.70	1.86×10^{20}
graphite	56.27	2.70×10^{20}
greenalite	129.35	6.24×10^{20}
pyrite	72.31	3.47×10^{20}
quartz	220.73	1.06×10^{21}
talc	79.33	3.81×10^{20}
tobermorite	0.02	1.10×10^{17}
	Mean density kg/m^3	Thickness km
Total precipitates	2881[a]	38.20[a]
Gases exsolved	Concentration g/kg fluid	Mass kg
CH_4 gas	38.84	1.86×10^{20}
	Mass kg	A_{Hyd}/M_{Eur} Mass %
Adjusted hydrosphere (A_{Hyd})	4.61×10^{21}	9.61

[a]Does not include tobermorite precipitated, since it is not thermodynamically stable at the seafloor (see Fig. S15).

Figure S16: Final radial properties of Europa

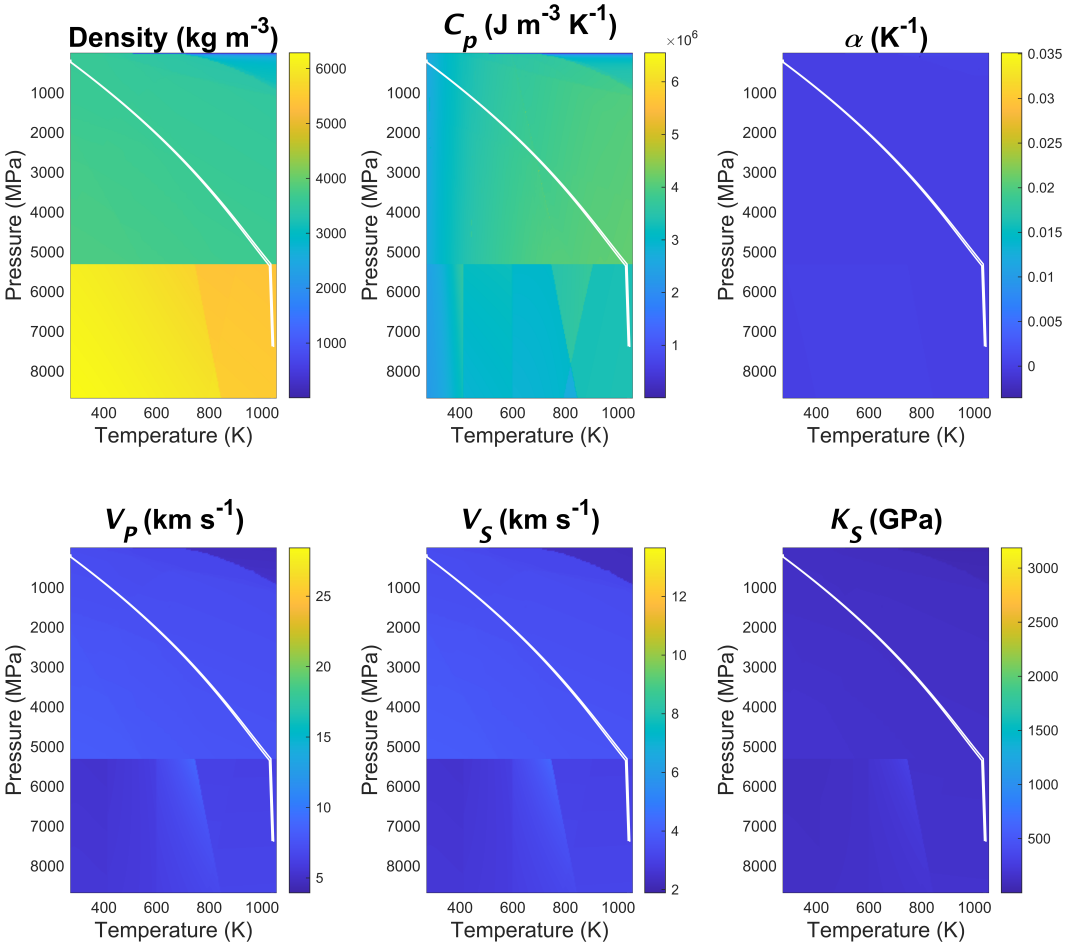

Figure 16. Radial properties and structure of the interior of Europa for an ocean with the properties of seawater. White curves are pressure-temperature profiles corresponding to a Europa with a $\sim$ 5 km surface ice Ih shell (slightly warmer, i.e., steeper profile) and a $\sim$ 30 km surface ice Ih shell (slightly cooler).

References

Airieau, S., Farquhar, J., Thiemens, M., Leshin, L., Bao, H., & Young, E. (2005, August). Planetesimal sulfate and aqueous alteration in CM and CI carbonaceous chondrites. *Geochimica et Cosmochimica Acta*, *69*(16), 4167–4172. Retrieved from http://www.sciencedirect.com/science/article/pii/S0016703705002437 doi: 10.1016/j.gca.2005.01.029

Anderson, J. D., Schubert, G., Jacobson, R. A., Lau, E. L., Moore, W. B., & Sjogren, W. L. (1998). Europa's differentiated internal structure: Inferences from four Galileo encounters. *Science*, *281*(5385), 2019–2022. Retrieved from http://science.sciencemag.org/content/281/5385/2019 doi: 10.1126/science.281.5385.2019

Badro, J., Brodholt, J. P., Piet, H., Siebert, J., & Ryerson, F. J. (2015). Core formation and core composition from coupled geochemical and geophysical constraints. *Proceedings of the National Academy of Sciences of the United States of America*, *112*(40), 12310–12314. Retrieved from http://www.ncbi.nlm.nih.gov/pmc/articles/PMC4603515/ doi: 10.1073/pnas.1505672112

Bardyn, A., Baklouti, D., Cottin, H., Fray, N., Briois, C., Paquette, J., ... Hilchenbach, M. (2017, July). Carbon-rich dust in comet 67P/Churyumov-Gerasimenko measured by COSIMA/Rosetta. *Monthly Notices of the Royal Astronomical Society*, *469*(Suppl_2), S712–S722. Retrieved 2020-06-25, from https://academic.oup.com/mnras/article/469/Suppl_2/S712/4670835 doi: 10.1093/mnras/stx2640

Bjerga, A. (2014). *Evolution of talc- and carbonate-bearing alterations in ultramafic rocks on Leka (central Norway)* (Doctoral dissertation, The University of Bergen, Bergen). Retrieved 2021-04-04, from https://hdl.handle.net/1956/7893 (Accepted: 2014-04-01T07:58:09Z Publisher: The University of Bergen)

Bjerga, A., Konopásek, J., & Pedersen, R. (2015, June). Talc–carbonate alteration of ultramafic rocks within the Leka Ophiolite Complex, Central Norway. *Lithos*, *227*, 21–36. Retrieved from https://www.sciencedirect.com/science/article/pii/S0024493715001085 doi: 10.1016/j.lithos.2015.03.016

Bland, P. A., Cressey, G., & Menzies, O. N. (2004, January). Modal mineralogy of carbonaceous chondrites by X-ray diffraction and Mössbauer spectroscopy. *Meteoritics & Planetary Science*, *39*(1), 3–16. Retrieved 2020-03-04, from https://doi.org/10.1111/j.1945-5100.2004.tb00046.x (Publisher: John Wiley & Sons, Ltd) doi: 10.1111/j.1945-5100.2004.tb00046.x

Bouquet, A., Mousis, O., Glein, C. R., Danger, G., & Waite, J. H. (2019, oct). The role of clathrate formation in europa's ocean composition. *The Astrophysical Journal*, *885*(1), 14. Retrieved from https://doi.org/10.3847%2F1538-4357%2Fab40b0 doi: 10.3847/1538-4357/ab40b0

Brearley, A. J. (2006, January). The Action of Water. In *Meteorites and the Early Solar System II* (p. 584). Retrieved from https://ui.adsabs.harvard.edu/abs/2006mess.book..584B (Journal Abbreviation: Meteorites and the Early Solar System II)

Bretscher, A., Hermann, J., & Pettke, T. (2018, October). The influence of oceanic oxidation on serpentinite dehydration during subduction. *Earth and Planetary Science Letters*, *499*, 173–184. Retrieved from https://www.sciencedirect.com/science/article/pii/S0012821X18304230 doi: 10.1016/j.epsl.2018.07.017

Běhounková, M., Tobie, G., Choblet, G., Kervazo, M., Melwani Daswani, M., Dumoulin, C., & Vance, S. D. (2021, February). Tidally Induced Mag-

matic Pulses on the Oceanic Floor of Jupiter's Moon Europa. *Geophysical Research Letters*, *48*(3), e2020GL090077. Retrieved 2021-02-05, from https://doi.org/10.1029/2020GL090077 (Publisher: John Wiley & Sons, Ltd) doi: 10.1029/2020GL090077

Canup, R. M., & Ward, W. R. (2009). Origin of Europa and the Galilean satellites. In R. T. Pappalardo, W. B. McKinnon, & K. Khurana (Eds.), *Europa* (pp. 59–83). Tucson, AZ: University of Arizona Press.

Cerpa, N. G., Padrón-Navarta, J. A., & Arcay, D. (2020, March). Uncertainties in the stability field of UHP hydrous phases (10-A phase and phase E) and deep-slab dehydration: potential implications for fluid migration and water fluxes at subduction zones.. Retrieved 2021-04-04, from https://meetingorganizer.copernicus.org/EGU2020/EGU2020-4783.html doi: 10.5194/egusphere-egu2020-4783

Chatterjee, N. D., & Froese, E. (1975, December). A thermodynamic study of the pseudobinary join muscovite-paragonite in the system KAlSi3O8-NaAlSi3O8-Al2O3-SiO2-H2O. *American Mineralogist*, *60*(11-12), 985–993.

Choblet, G., Tobie, G., Sotin, C., Kalousová, K., & Grasset, O. (2017, March). Heat transport in the high-pressure ice mantle of large icy moons. *Icarus*, *285*, 252–262. Retrieved from http://www.sciencedirect.com/science/article/pii/S0019103516302524 doi: 10.1016/j.icarus.2016.12.002

Clay, P. L., Burgess, R., Busemann, H., Ruzié-Hamilton, L., Joachim, B., Day, J. M. D., & Ballentine, C. J. (2017, November). Halogens in chondritic meteorites and terrestrial accretion. *Nature*, *551*(7682), 614–618. Retrieved from https://doi.org/10.1038/nature24625 doi: 10.1038/nature24625

Connolly, J. A. D. (2005). Computation of phase equilibria by linear programming: A tool for geodynamic modeling and its application to subduction zone decarbonation. *Earth and Planetary Science Letters*, *236*(1-2), 524–541. Retrieved 2018-08-08, from http://linkinghub.elsevier.com/retrieve/pii/S0012821X05002839 doi: 10.1016/j.epsl.2005.04.033

Connolly, J. A. D. (2009). The geodynamic equation of state: What and how. *Geochemistry, Geophysics, Geosystems*, *10*(10). Retrieved 2018-03-22, from https://agupubs.onlinelibrary.wiley.com/doi/abs/10.1029/2009GC002540 doi: 10.1029/2009GC002540

Connolly, J. A. D., & Galvez, M. E. (2018). Electrolytic fluid speciation by Gibbs energy minimization and implications for subduction zone mass transfer. *Earth and Planetary Science Letters*, *501*, 90–102. Retrieved 2019-01-07, from https://linkinghub.elsevier.com/retrieve/pii/S0012821X18304904 doi: 10.1016/j.epsl.2018.08.024

Connolly, J. A. D., & Podladchikov, Y. Y. (1998, March). Compaction-driven fluid flow in viscoelastic rock. *Geodinamica Acta*, *11*(2-3), 55–84. Retrieved from https://www.tandfonline.com/doi/abs/10.1080/09853111.1998.11105311 (Publisher: Taylor & Francis) doi: 10.1080/09853111.1998.11105311

Craddock, R. A., & Greeley, R. (2009, December). Minimum estimates of the amount and timing of gases released into the martian atmosphere from volcanic eruptions. *Icarus*, *204*(2), 512–526. Retrieved from http://www.sciencedirect.com/science/article/pii/S001910350900311X doi: 10.1016/j.icarus.2009.07.026

Day, J. M., Corder, C. A., Assayag, N., & Cartigny, P. (2019). Ferrous oxide-rich asteroid achondrites. *Geochimica et Cosmochimica Acta*. Retrieved from http://www.sciencedirect.com/science/article/pii/S0016703719302121 doi: 10.1016/j.gca.2019.04.005

Desch, S. J., Kalyaan, A., & Alexander, C. M. O. (2018). The Effect of Jupiter's Formation on the Distribution of Refractory Elements and Inclusions in Me-

teorites. *The Astrophysical Journal Supplement Series*, *238*(1), 11. Retrieved from http://stacks.iop.org/0067-0049/238/i=1/a=11

Dhooghe, F., De Keyser, J., Altwegg, K., Briois, C., Balsiger, H., Berthelier, J.-J., ... Wurz, P. (2017, December). Halogens as tracers of protosolar nebula material in comet 67P/Churyumov–Gerasimenko. *Monthly Notices of the Royal Astronomical Society*, *472*(2), 1336–1345. Retrieved 2020-06-25, from http://academic.oup.com/mnras/article/472/2/1336/4062198/Halogens-as-tracers-of-protosolar- doi: 10.1093/mnras/stx1911

Erkaev, N., Lammer, H., Elkins-Tanton, L., Stökl, A., Odert, P., Marcq, E., ... Güdel, M. (2014, August). Escape of the martian protoatmosphere and initial water inventory. *Planetary evolution and life*, *98*, 106–119. Retrieved from http://www.sciencedirect.com/science/article/pii/S0032063313002353 doi: 10.1016/j.pss.2013.09.008

Estrada, P. R., Mosqueira, I., Lissauer, J. J., D'Angelo, G., & Cruikshank, D. (2009). Formation of Jupiter and conditions for accretion of the Galilean satellites. In R. T. Pappalardo, W. B. McKinnon, & K. Khurana (Eds.), *Europa* (pp. 27–58). Tucson, AZ: University of Arizona Press.

Ferrand, T. P., Hilairet, N., Incel, S., Deldicque, D., Labrousse, L., Gasc, J., ... Schubnel, A. (2017, May). Dehydration-driven stress transfer triggers intermediate-depth earthquakes. *Nature Communications*, *8*(1), 15247. Retrieved from https://doi.org/10.1038/ncomms15247 doi: 10.1038/ncomms15247

Flynn, G. J., Consolmagno, G. J., Brown, P., & Macke, R. J. (2018, September). Physical properties of the stone meteorites: Implications for the properties of their parent bodies. *Geochemistry*, *78*(3), 269–298. Retrieved 2020-06-25, from https://linkinghub.elsevier.com/retrieve/pii/S0009281916302860 doi: 10.1016/j.chemer.2017.04.002

Fowler, A. P., Zierenberg, R. A., Reed, M. H., Palandri, J., Óskarsson, F., & Gunnarsson, I. (2019, January). Rare earth element systematics in boiled fluids from basalt-hosted geothermal systems. *Geochimica et Cosmochimica Acta*, *244*, 129–154. Retrieved from http://www.sciencedirect.com/science/article/pii/S0016703718305751 doi: 10.1016/j.gca.2018.10.001

Fredriksson, K., & Kerridge, J. F. (1988, March). Carbonates and sulfates in CI chondrites - Formation by aqueous activity on the parent body. *Meteoritics*, *23*, 35–44.

Freedman, A. J. E., Bird, D. K., Arnorsson, S., Fridriksson, T., Elders, W. A., & Fridleifsson, G. O. (2009, November). Hydrothermal minerals record CO2 partial pressures in the Reykjanes geothermal system, Iceland. *American Journal of Science*, *309*(9), 788–833. Retrieved 2020-10-13, from http://www.ajsonline.org/cgi/doi/10.2475/09.2009.02 doi: 10.2475/09.2009.02

Frost, B. R. (1991, December). Chapter 1. Introduction to oxygen fugacity and its petrological importance. In D. H. Lindsley (Ed.), *Oxide Minerals* (pp. 1–10). Berlin, Boston: De Gruyter. Retrieved 2021-03-19, from https://www.degruyter.com/document/doi/10.1515/9781501508684-004/html doi: 10.1515/9781501508684-004

García-Arias, M. (2020, December). Consistency of the activity–composition models of Holland, Green, and Powell (2018) with experiments on natural and synthetic compositions: A comparative study. *Journal of Metamorphic Geology*, *38*(9), 993–1010. Retrieved 2021-04-05, from https://doi.org/10.1111/jmg.12557 (Publisher: John Wiley & Sons, Ltd) doi: 10.1111/jmg.12557

Gorce, J., Caddick, M., & Bodnar, R. (2019, August). Thermodynamic constraints on carbonate stability and carbon volatility during subduction.

Earth and Planetary Science Letters, *519*, 213–222. Retrieved from https://www.sciencedirect.com/science/article/pii/S0012821X19302596 doi: 10.1016/j.epsl.2019.04.047

Gounelle, M., & Zolensky, M. E. (2001, October). A terrestrial origin for sulfate veins in CI1 chondrites. *Meteoritics & Planetary Science*, *36*(10), 1321–1329. Retrieved 2020-04-06, from https://doi.org/10.1111/j.1945-5100.2001.tb01827.x (Publisher: John Wiley & Sons, Ltd) doi: 10.1111/j.1945-5100.2001.tb01827.x

Green, E., Holland, T. J. B., & Powell, R. (2007, July). An order-disorder model for omphacitic pyroxenes in the system jadeite-diopside-hedenbergite-acmite, with applications to eclogitic rocks. *American Mineralogist*, *92*(7), 1181–1189. Retrieved 2020-06-27, from https://pubs.geoscienceworld.org/ammin/article/92/7/1181-1189/134540 doi: 10.2138/am.2007.2401

Hansen, G. B., & McCord, T. B. (2008, January). Widespread CO2 and other non-ice compounds on the anti-Jovian and trailing sides of Europa from Galileo/NIMS observations. *Geophysical Research Letters*, *35*(1). Retrieved 2020-10-08, from https://doi.org/10.1029/2007GL031748 (Publisher: John Wiley & Sons, Ltd) doi: 10.1029/2007GL031748

Holland, T. J. B., Baker, J., & Powell, R. (1998, 06). Mixing properties and activity-composition relationships of chlorites in the system mgo-feo-al2o3-sio2-h2o. *European Journal of Mineralogy*, *10*(3), 395-406. Retrieved from http://dx.doi.org/10.1127/ejm/10/3/0395 doi: 10.1127/ejm/10/3/0395

Holland, T. J. B., Green, E. C. R., & Powell, R. (2018, May). Melting of Peridotites through to Granites: A Simple Thermodynamic Model in the System KNCF-MASHTOCr. *Journal of Petrology*, *59*(5), 881–900. Retrieved 2019-01-07, from https://academic.oup.com/petrology/article/59/5/881/4996852 doi: 10.1093/petrology/egy048

Hussmann, H., & Spohn, T. (2004). Thermal-orbital evolution of Io and Europa. *Icarus*, *171*(2), 391 - 410. Retrieved from http://www.sciencedirect.com/science/article/pii/S0019103504001952 doi: https://doi.org/10.1016/j.icarus.2004.05.020

Jennings, E. S., Holland, T. J. B., Shorttle, O., Maclennan, J., & Gibson, S. A. (2016, December). The Composition of Melts from a Heterogeneous Mantle and the Origin of Ferropicrite: Application of a Thermodynamic Model. *Journal of Petrology*, egw065. Retrieved 2020-06-27, from https://academic.oup.com/petrology/article-lookup/doi/10.1093/petrology/egw065 doi: 10.1093/petrology/egw065

Jia, X., Kivelson, M. G., Khurana, K. K., & Kurth, W. S. (2018, June). Evidence of a plume on Europa from Galileo magnetic and plasma wave signatures. *Nature Astronomy*, *2*(6), 459–464. Retrieved from https://doi.org/10.1038/s41550-018-0450-z doi: 10.1038/s41550-018-0450-z

Kalousová, K., & Sotin, C. (2020, September). Dynamics of Titan's high-pressure ice layer. *Earth and Planetary Science Letters*, *545*, 116416. Retrieved from http://www.sciencedirect.com/science/article/pii/S0012821X20303605 doi: 10.1016/j.epsl.2020.116416

Kuramoto, K., & Matsui, T. (1994, October). Formation of a hot proto-atmosphere on the accreting giant icy satellite: Implications for the origin and evolution of Titan, Ganymede, and Callisto. *Journal of Geophysical Research: Planets*, *99*(E10), 21183–21200. Retrieved 2021-01-29, from https://doi.org/10.1029/94JE01864 (Publisher: John Wiley & Sons, Ltd) doi: 10.1029/94JE01864

Kuskov, O., & Kronrod, V. (2005). Internal structure of Europa and Callisto. *Icarus*, *177*(2), 550 - 569. Retrieved from

http://www.sciencedirect.com/science/article/pii/S0019103505001806 doi: https://doi.org/10.1016/j.icarus.2005.04.014

Lammer, H., Chassefière, E., Karatekin, O., Morschhauser, A., Niles, P. B., Mousis, O., ... Pham, L. (2013, January). Outgassing History and Escape of the Martian Atmosphere and Water Inventory. *Space Science Reviews*, *174*(1-4), 113–154. Retrieved from http://dx.doi.org/10.1007/s11214-012-9943-8 doi: 10.1007/s11214-012-9943-8

Lammer, H., Selsis, F., Chassefière, E., Breuer, D., Grießmeier, J.-M., Kulikov, Y. N., ... White, G. J. (2010, January). Geophysical and Atmospheric Evolution of Habitable Planets. *Astrobiology*, *10*(1), 45–68. Retrieved 2021-04-13, from http://www.liebertpub.com/doi/10.1089/ast.2009.0368 doi: 10.1089/ast.2009.0368

Leclère, H., Faulkner, D., Llana-Fúnez, S., Bedford, J., & Wheeler, J. (2018, August). Reaction fronts, permeability and fluid pressure development during dehydration reactions. *Earth and Planetary Science Letters*, *496*, 227–237. Retrieved 2020-06-26, from https://linkinghub.elsevier.com/retrieve/pii/S0012821X18302759 doi: 10.1016/j.epsl.2018.05.005

Le Roy, L., Altwegg, K., Balsiger, H., Berthelier, J.-J., Bieler, A., Briois, C., ... Tzou, C.-Y. (2015, November). Inventory of the volatiles on comet 67P/Churyumov-Gerasimenko from Rosetta/ROSINA. *Astronomy & Astrophysics*, *583*, A1. Retrieved 2020-06-25, from http://www.aanda.org/10.1051/0004-6361/201526450 doi: 10.1051/0004-6361/201526450

Li, J., & Fei, Y. (2014). 3.15 - Experimental constraints on core composition. In H. D. Holland & K. K. Turekian (Eds.), *Treatise on geochemistry* (Second ed., p. 527 - 557). Oxford: Elsevier. Retrieved from http://www.sciencedirect.com/science/article/pii/B978008095975700214X doi: https://doi.org/10.1016/B978-0-08-095975-7.00214-X

Lodders, K., & Fegley, B. (1998). *The planetary scientist's companion.* New York: Oxford University Press.

Lunine, J. I., & Nolan, M. C. (1992, November). A massive early atmosphere on Triton. *Icarus*, *100*(1), 221–234. Retrieved from http://www.sciencedirect.com/science/article/pii/0019103592900312 doi: 10.1016/0019-1035(92)90031-2

Mayne, M. J., Moyen, J.-F., Stevens, G., & Kaislaniemi, L. (2016, May). Rcrust: a tool for calculating path-dependent open system processes and application to melt loss. *Journal of Metamorphic Geology*, *34*(7), 663–682. Retrieved 2018-07-25, from https://doi.org/10.1111/jmg.12199 doi: 10.1111/jmg.12199

McCord, T. B., Hansen, G. B., Fanale, F. P., Carlson, R. W., Matson, D. L., Johnson, T. V., ... Granahan, J. C. (1998, May). Salts on Europa's Surface Detected by Galileo's Near Infrared Mapping Spectrometer. *Science*, *280*(5367), 1242. Retrieved from http://science.sciencemag.org/content/280/5367/1242.abstract doi: 10.1126/science.280.5367.1242

McCord, T. B., Hansen, G. B., Matson, D. L., Johnson, T. V., Crowley, J. K., Fanale, F. P., ... Ocampo, A. (1999, May). Hydrated salt minerals on Europa's surface from the Galileo near-infrared mapping spectrometer (NIMS) investigation. *Journal of Geophysical Research: Planets*, *104*(E5), 11827–11851. Retrieved 2020-10-08, from https://doi.org/10.1029/1999JE900005 (Publisher: John Wiley & Sons, Ltd) doi: 10.1029/1999JE900005

McKinnon, W. B., & Zolensky, M. E. (2003). Sulfate Content of Europa's Ocean and Shell: Evolutionary Considerations and Some Geological and Astrobiological Implications. *Astrobiology*, *3*(4), 879–897. Retrieved 2020-04-06, from https://doi.org/10.1089/153110703322736150 (Publisher: Mary Ann

Liebert, Inc., publishers) doi: 10.1089/153110703322736150

Menzel, M. D., Garrido, C. J., & López Sánchez-Vizcaíno, V. (2020, February). Fluid-mediated carbon release from serpentinite-hosted carbonates during dehydration of antigorite-serpentinite in subduction zones. *Earth and Planetary Science Letters*, *531*, 115964. Retrieved from https://www.sciencedirect.com/science/article/pii/S0012821X19306569 doi: 10.1016/j.epsl.2019.115964

Miller, S., van der Zee, W., Olgaard, D., & Connolly, J. (2003, July). A fluid-pressure feedback model of dehydration reactions: experiments, modelling, and application to subduction zones. *Physical Properties of Rocks and other Geomaterials, a Special Volume to honour Professor H. Kern*, *370*(1), 241–251. Retrieved from http://www.sciencedirect.com/science/article/pii/S0040195103001896 doi: 10.1016/S0040-1951(03)00189-6

Nozaka, T., Wintsch, R. P., & Meyer, R. (2017, June). Serpentinization of olivine in troctolites and olivine gabbros from the Hess Deep Rift. *Lithos*, *282-283*, 201–214. Retrieved from https://www.sciencedirect.com/science/article/pii/S0024493716304674 doi: 10.1016/j.lithos.2016.12.032

Odert, P., Lammer, H., Erkaev, N., Nikolaou, A., Lichtenegger, H., Johnstone, C., ... Tosi, N. (2018, June). Escape and fractionation of volatiles and noble gases from Mars-sized planetary embryos and growing protoplanets. *Icarus*, *307*, 327–346. Retrieved from http://www.sciencedirect.com/science/article/pii/S0019103517301677 doi: 10.1016/j.icarus.2017.10.031

Padrón-Navarta, J. A., Sánchez-Vizcaíno, V. L., Hermann, J., Connolly, J. A., Garrido, C. J., Gómez-Pugnaire, M. T., & Marchesi, C. (2013, September). Tschermak's substitution in antigorite and consequences for phase relations and water liberation in high-grade serpentinites. *Serpentinites from mid-oceanic ridges to subduction*, *178*, 186–196. Retrieved from http://www.sciencedirect.com/science/article/pii/S0024493713000327 doi: 10.1016/j.lithos.2013.02.001

Palandri, J. L., & Reed, M. H. (2004, March). Geochemical models of metasomatism in ultramafic systems: serpentinization, rodingitization, and sea floor carbonate chimney precipitation. *Geochimica et Cosmochimica Acta*, *68*(5), 1115–1133. Retrieved from http://www.sciencedirect.com/science/article/pii/S0016703703005921 doi: 10.1016/j.gca.2003.08.006

Palme, H., Lodders, K., & Jones, A. (2014, January). 2.2 - Solar System Abundances of the Elements. In H. D. Holland & K. K. Turekian (Eds.), *Treatise on Geochemistry (Second Edition)* (pp. 15–36). Oxford: Elsevier. Retrieved from http://www.sciencedirect.com/science/article/pii/B9780080959757001182 doi: 10.1016/B978-0-08-095975-7.00118-2

Pan, D., Spanu, L., Harrison, B., Sverjensky, D. A., & Galli, G. (2013, April). Dielectric properties of water under extreme conditions and transport of carbonates in the deep Earth. *Proceedings of the National Academy of Sciences*, *110*(17), 6646. Retrieved from http://www.pnas.org/content/110/17/6646.abstract doi: 10.1073/pnas.1221581110

Pätzold, M., Andert, T., Hahn, M., Asmar, S. W., Barriot, J.-P., Bird, M. K., ... Scholten, F. (2016, February). A homogeneous nucleus for comet 67P/Churyumov–Gerasimenko from its gravity field. *Nature*, *530*(7588), 63–65. Retrieved 2020-06-25, from http://www.nature.com/articles/nature16535 doi: 10.1038/nature16535

Pitzer, K. S., & Sterner, S. M. (1994, August). Equations of state valid con-

tinuously from zero to extreme pressures for H $_2$ O and CO $_2$. *The Journal of Chemical Physics*, *101*(4), 3111–3116. Retrieved 2021-04-13, from http://aip.scitation.org/doi/10.1063/1.467624 doi: 10.1063/1.467624

Prieto-Ballesteros, O., Kargel, J. S., Fernández-Sampedro, M., Selsis, F., Martínez, E. S., & Hogenboom, D. L. (2005, October). Evaluation of the possible presence of clathrate hydrates in Europa's icy shell or seafloor. *Europa Icy Shell*, *177*(2), 491–505. Retrieved from http://www.sciencedirect.com/science/article/pii/S0019103505001351 doi: 10.1016/j.icarus.2005.02.021

Reed, M. H. (1998). Calculation of simultaneous chemical equilibria in aqueous-mineral-gas systems and its application to modeling hydrothermal processes. In J. P. Richards (Ed.), *Techniques in Hydrothermal Ore Deposits Geology* (Vol. 10, pp. 109–124). Littleton, CO: Society of Economic Geologists, Inc.

Richard, G., Monnereau, M., & Rabinowicz, M. (2007, March). Slab dehydration and fluid migration at the base of the upper mantle: implications for deep earthquake mechanisms. *Geophysical Journal International*, *168*(3), 1291–1304. Retrieved 2020-06-27, from https://doi.org/10.1111/j.1365-246X.2006.03244.x doi: 10.1111/j.1365-246X.2006.03244.x

Ronnet, T., Mousis, O., & Vernazza, P. (2017). Pebble Accretion at the Origin of Water in Europa. *The Astrophysical Journal*, *845*(2), 92. Retrieved 2018-12-18, from http://stacks.iop.org/0004-637X/845/i=2/a=92?key=crossref.e075ce27e4a38f6e8b1624cbb3608530 doi: 10.3847/1538-4357/aa80e6

Roth, L., Saur, J., Retherford, K. D., Strobel, D. F., Feldman, P. D., McGrath, M. A., & Nimmo, F. (2014, January). Transient Water Vapor at Europa's South Pole. *Science*, *343*(6167), 171. Retrieved from http://science.sciencemag.org/content/343/6167/171.abstract doi: 10.1126/science.1247051

Saxena, S., & Eriksson, G. (2015). Thermodynamics of Fe-S at ultra-high pressure. *Calphad*, *51*, 202 - 205. Retrieved from http://www.sciencedirect.com/science/article/pii/S0364591615300249 doi: https://doi.org/10.1016/j.calphad.2015.09.009

Schubert, G., Sohl, F., & Hussmann, H. (2009). Interior of Europa. In R. T. Pappalardo, W. B. McKinnon, & K. Khurana (Eds.), *Europa* (pp. 353–367). Tucson: University of Arizona Press.

Scott, H., Williams, Q., & Ryerson, F. (2002). Experimental constraints on the chemical evolution of large icy satellites. *Earth and Planetary Science Letters*, *203*(1), 399 - 412. Retrieved from http://www.sciencedirect.com/science/article/pii/S0012821X02008506 doi: https://doi.org/10.1016/S0012-821X(02)00850-6

Singerling, S. A., & Brearley, A. J. (2018). Primary iron sulfides in CM and CR carbonaceous chondrites: Insights into nebular processes. *Meteoritics & Planetary Science*, *53*(10), 2078–2106. Retrieved 2020-03-04, from https://doi.org/10.1111/maps.13108 (Publisher: John Wiley & Sons, Ltd) doi: 10.1111/maps.13108

Sloan, E. D., & Koh, C. A. (2008). *Clathrate hydrates of natural gases* (3. ed ed.) (No. 119). Boca Raton, FL: CRC Press, Taylor & Francis. (OCLC: 836511793)

Sohl, F., Spohn, T., Breuer, D., & Nagel, K. (2002). Implications from galileo observations on the interior structure and chemistry of the galilean satellites. *Icarus*, *157*(1), 104 - 119. Retrieved from http://www.sciencedirect.com/science/article/pii/S0019103502968284 doi: https://doi.org/10.1006/icar.2002.6828

Sonzogni, Y., Treiman, A. H., & Schwenzer, S. P. (2017). Serpentinite with

and without brucite: A reaction pathway analysis of a natural serpentinite in the Josephine ophiolite, California. *Journal of Mineralogical and Petrological Sciences*, *112*(2), 59–76. Retrieved 2021-04-14, from https://www.jstage.jst.go.jp/article/jmps/112/2/112_160509/_-article doi: 10.2465/jmps.160509

Sotin, C., Grasset, O., & Mocquet, A. (2007). Mass-radius curve for extrasolar Earth-like planets and ocean planets. *Icarus*, *191*(1), 337–351. Retrieved 2018-10-23, from http://linkinghub.elsevier.com/retrieve/pii/S0019103507001601 doi: 10.1016/j.icarus.2007.04.006

Sotin, C., & Tobie, G. (2004). Internal structure and dynamics of the large icy satellites. *Comptes Rendus Physique*, *5*(7), 769 - 780. Retrieved from http://www.sciencedirect.com/science/article/pii/S163107050400146X doi: https://doi.org/10.1016/j.crhy.2004.08.001

Sparks, W. B., Hand, K. P., McGrath, M. A., Bergeron, E., Cracraft, M., & Deustua, S. E. (2016, September). Probing for evidence of plumes on Europa with HST/STIS. *The Astrophysical Journal*, *829*(2), 121. Retrieved from http://dx.doi.org/10.3847/0004-637X/829/2/121 (Publisher: American Astronomical Society) doi: 10.3847/0004-637x/829/2/121

Steenstra, E. S., & van Westrenen, W. (2018). A synthesis of geochemical constraints on the inventory of light elements in the core of Mars. *Icarus*, *315*, 69 - 78. Retrieved from http://www.sciencedirect.com/science/article/pii/S0019103518302045 doi: https://doi.org/10.1016/j.icarus.2018.06.023

Sverjensky, D. A., Harrison, B., & Azzolini, D. (2014, March). Water in the deep Earth: The dielectric constant and the solubilities of quartz and corundum to 60kb and 1200°C. *Geochimica et Cosmochimica Acta*, *129*, 125–145. Retrieved from http://www.sciencedirect.com/science/article/pii/S0016703713007151 doi: 10.1016/j.gca.2013.12.019

Tian, F., Kasting, J. F., & Solomon, S. C. (2009, January). Thermal escape of carbon from the early Martian atmosphere. *Geophysical Research Letters*, *36*(2). Retrieved 2021-04-03, from https://doi.org/10.1029/2008GL036513 (Publisher: John Wiley & Sons, Ltd) doi: 10.1029/2008GL036513

Tobie, G., Choblet, G., & Sotin, C. (2003). Tidally heated convection: Constraints on Europa's ice shell thickness. *Journal of Geophysical Research: Planets*, *108*(E11). Retrieved 2019-01-08, from https://doi.org/10.1029/2003JE002099 doi: 10.1029/2003JE002099

Tobie, G., Mocquet, A., & Sotin, C. (2005). Tidal dissipation within large icy satellites: Applications to Europa and Titan. *Europa Icy Shell*, *177*(2), 534–549. Retrieved from http://www.sciencedirect.com/science/article/pii/S0019103505001582 doi: 10.1016/j.icarus.2005.04.006

Vance, S. D., Panning, M. P., Stähler, S., Cammarano, F., Bills, B. G., Tobie, G., ... Banerdt, B. (2018). Geophysical investigations of habitability in ice-covered ocean worlds. *Journal of Geophysical Research: Planets*, *123*(1), 180-205. Retrieved from https://agupubs.onlinelibrary.wiley.com/doi/abs/10.1002/2017JE005341 doi: 10.1002/2017JE005341

Verba, C., O'Connor, W., Rush, G., Palandri, J., Reed, M., & Ideker, J. (2014, April). Geochemical alteration of simulated wellbores of CO2 injection sites within the Illinois and Pasco Basins. *International Journal of Greenhouse Gas Control*, *23*, 119–134. Retrieved from http://www.sciencedirect.com/science/article/pii/S1750583614000309 doi: 10.1016/j.ijggc.2014.01.015

Walder, P., & Pelton, A. D. (2005). Thermodynamic modeling of the Fe-S system. *Journal of Phase Equilibria and Diffusion*, *26*(1), 23–38. Retrieved from https://doi.org/10.1007/s11669-005-0055-y doi: 10.1007/s11669-005-0055-y

Warner, M. (2004, March). Free water and seismic reflectivity in the lower continental crust. *Journal of Geophysics and Engineering*, *1*(1), 88–101. Retrieved 2021-04-06, from https://doi.org/10.1088/1742-2132/1/1/012 doi: 10.1088/1742-2132/1/1/012

Wilson, C. R., Spiegelman, M., van Keken, P. E., & Hacker, B. R. (2014, September). Fluid flow in subduction zones: The role of solid rheology and compaction pressure. *Earth and Planetary Science Letters*, *401*, 261–274. Retrieved 2020-06-26, from https://linkinghub.elsevier.com/retrieve/pii/S0012821X14003628 doi: 10.1016/j.epsl.2014.05.052

Wood, B. J., Li, J., & Shahar, A. (2013). Carbon in the core: Its influence on the properties of core and mantle. *Reviews in Mineralogy and Geochemistry*, *75*(1), 231. Retrieved from http://dx.doi.org/10.2138/rmg.2013.75.8 doi: 10.2138/rmg.2013.75.8

Zhang, H. (2003). Internal structure models and dynamical parameters of the Galilean satellites. *Celestial Mechanics and Dynamical Astronomy*, *87*(1), 189–195. Retrieved from https://doi.org/10.1023/A:1026188029324 doi: 10.1023/A:1026188029324

Zolensky, M., Barrett, R., & Browning, L. (1993, July). Mineralogy and composition of matrix and chondrule rims in carbonaceous chondrites. *Geochimica et Cosmochimica Acta*, *57*(13), 3123–3148. Retrieved from https://www.sciencedirect.com/science/article/pii/001670379390298B doi: 10.1016/0016-7037(93)90298-B

Zolotov, M. Y., & Kargel, J. S. (2009). On the chemical composition of Europa's icy shell, ocean, and underlying rocks. In R. T. Pappalardo, W. B. McKinnon, & K. Khurana (Eds.), *Europa* (p. 431). University of Arizona Press Tucson, AZ. Retrieved from https://uapress.arizona.edu/book/europa